Active Optical Phase-Change Plasmonic Transdimensional Systems Enabling Femtojoule and Femtosecond Extreme Broadband Adaptive Reconfigurable Devices

Grant Agreement No: 899598

Deliverable D2.1

Analysis of Synthesized Phase Change Materials

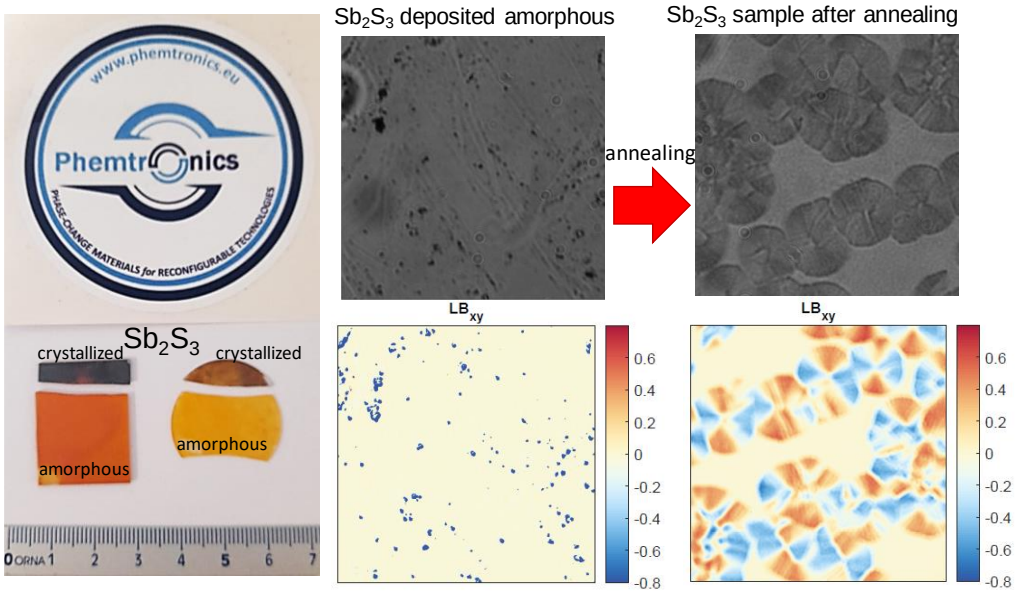

Deliverable type:	REPORT
Deliverable reference number:	899598 / D2.1./ v.1.0
Deliverable title:	ANALYSIS OF SYNTHETIZED PHASE CHANGE MATERIALS
WP contributing to the deliverable:	WP2
Dissemination level	Public
Responsible Editor:	CNR
Due date:	30105/2021 (M12)
Actual submission date:	24/06/2021 (M13)

Start of the Project: June 1st, 2020	**Duration: 36 months**
Coordinator: Maria Losurdo, CNR-NANOTEC	Contact: maria.losurdo@cnr.it coordinator@phemtronics.eu
Project website	**www.phemtronics.eu**

Authors List

Organization	Author(s)
CNR	Dr. Maria Losurdo, Dr. Yael Gutiérrez, Dr. Maria M. Giangregorio, Dr. Sterano Dicorato, Dr. Giuseppe V. Bianco, Dr. Alberto Perrotta, Dr. Fabio Palumbo
UCC-Tyndall	Dr. Mircea Modreanu
JKU	Dr. Christoph Cobet, Prof. Kurt Hingerl, DI. Mario Graml, DI. Josef Resl
UC	Prof. Fernando Moreno, Gonzalo Santos
NANOM	Prof. Marin Georghe, Prof. Cornel Cobianu

Cite this document as ©PHEMTRONICS e-BOOKLET (2021)

ISBN: 978-3-9504630-9-5

DOI: *(it will appear after Approval and upload in ZENODO Repository)*

Members of the PHEMTRONICS Consortium

CNR NANOTEC INSTITUTE OF NANOTECHNOLOGY	Istituto di Nanotecnologia Consiglio Nazionale delle Ricerche Via Amendola 12/D 70126 Bari, Italy www.nanotec.cnr.it	**Project Coordinator:** **Maria Losurdo** maria.losurdo@cnr.it coordinator@phemtronics.eu
Westfälische Wilhelms-Universität Münster	Westfaelische Wilhelmsuniversitaet Muenster Schlossplatz 2, 48149 Münster, Germany www.uni-muenster.de/en/	**Prof. Wolfram Pernice** wolfram.pernice@uni-muenster.de
Tyndall National Institute Institiúid Náisiúnta	University College Cork - National University Of Ireland, 1 Dyke Parade, Cork, T12 FE00, Ireland www.tyndall.ie	**Dr. Mircea Modreanu** mircea.modreanu@tyndall.ie
JKU JOHANNES KEPLER UNIVERSITÄT LINZ	Johannes Keppler University Altenbergerstraße 69, 4040 Linz, Austria www.jku.at/en/	**Dr. Christoph Cobet** Christoph.Cobet@jku.at
UC UNIVERSIDAD DE CANTABRIA	University of Cantabria Avda. Los Castros s/n Santander, 39005, Cantabria, Spain www.unican.es	**Prof. Fernando Moreno** fernando.moreno@unican.es
NANOM MEMS SRL	NANOM MEMS SRL Strada George Coșbuc 9 Râșnov 505400 Brașov, Romania www.nanom-mems.com	**Dr. Marin Gheorghe** maringhe@nanom-mems.com
TE-OX	TE-OX Parc Orsay Université 2 Rue Jean Rostand 91893 Orsay Cedex France www.te-ox.com	**Dr. Guy Garry** guy.garry@te-ox.com
VLC PHOTONICS	VLC PHOTONICS SOCIEDAD LIMITADA Building 9B , Office 0.71 Universidad Politécnica de Valencia Camino de Vera s/n, 46022 Valencia, Spain www.vlcphotonics.com	**Dr. Jordi Soler** jordi.soler@vlcphotonics.com

About Phemtronics

PHEMTRONICS was launched in June 2020 as a 3-year collaborative project on CMOS-compatible phase-change materials, plasmonic, photonic and electronic integration.

PHEMTRONICS aims at replacing "*slow*" electrical or thermal phase change materials with "*ultrafast*" "Optical-Phase-Change Plasmonic Materials", capable of self-reconfiguring and self-adapting as a response to light, shifting from current technology paradigms based on electronic switching to "all-optical switching" enabling broadband reconfigurability of devices.

PHEMTRONICS will enable a new technology paradigm of adaptive optical signal processing with ultrafast network reconfiguration with key metrics of the "femtosecond-scale switching time", "ultralow power of femtojoule/bit" and "microwave-to-optical frequencies" broadband capability required for reliable multibit operations. The exciting outcomes include demonstrations of:

- Ultrafast and low-power switches;
- Adaptive antennas;
- Adaptive switchable multiple-band detection for the future generation of photodetectors;
- All-optical spiking neuron circuit, with integrated all-optical synapses.

List of Abbreviations

2D = Two dimensional
AFM = Atomic Force Microscopy
ALD = Atomic Layer Deposition
CVD = Chemical Vapor Deposition
CBD = Chemical Bath Deposition
EDX = Energy Dispersive X-ray Spectroscopy
FTIR = Fourier Transmission Infrared Spectroscopy
GaS (Se) (Te) = Gallium Sulfide (Selenide) (Telluride)
GeS = Germanium Sulfide
GST = Germanium Antimony Telluride
MIT = Metal-Insulator-Transition
MoOx = Molibdenum Oxides
PCM = Phase Change Material
Sb_2S_3 = Antimony Sulfide
SE = Spectroscopic Ellipsometry
SEM = Scanning Electron Microscopy
TEM = Transmission Electron Microscopy
TMD = Transition Metal Dichalcogenide
XPS = X-ray Photoelectron Spectroscopy

Table of Contents

Executive Summary

Optical phase change materials (O-PCMs), a unique group of materials featuring exceptional optical property contrast upon a solid-state phase transition, have found widespread adoption in photonic applications such as switches, routers and reconfigurable meta-optics.
Nowadays, phase transition of materials is an important tuning mechanism exploited to design and fabricate reconfigurable photonic devices.
Phase transitions can be classified into various types, namely:

- insulator-metallic phase transition,
- amorphous–crystalline phase transition,
- phase transitions between various ordered configurations.

Strongly correlated materials like vanadium oxide undergo reversible, volatile metal-to-insulator phase transitions, while certain alloys like chalcogenides materials undergo non-volatile amorphous-to-crystalline phase transitions using an electrical, optical or thermal stimulus. Current O-PCMs, such as Ge–Sb–Te (GST), exhibit large contrast of both refractive index (Δ*n*) and optical loss (Δ*k*), simultaneously**,** by going through an amorphous, non-equilibrium, phase. The coupling of both optical properties fundamentally limits the performance of many applications

Several material platforms provide a unique route to tuning the optical response of metamaterials, where the geometry or refractive index of the meta-atom can be reversibly transitioned between two or more states exhibiting a distinct optical response

There is an intensive exploration of many material platforms, culminating in the identification of several suitable alloys with unique optical and material properties. A variety of germanium, gallium, antimony, and molybdenum alloyed chalcogenides are being explored in various nanophotonic devices.

Furthermore, two-dimensional (2D) materials, have emerged in the realization of reconfigurable devices. Consisting of a single atomic layer, they exhibit unique physical properties distinct from their three-dimensional counterparts. When various 2D crystals are stacked, they build so-called van der Waals heterostructures, which enable the engineering of artificial materials and devices with flexible properties. In particular, bandgap tuning of 2D materials, that is, engineering the size of the bandgap and even choosing between a direct and indirect gap, offers excellent opportunities for electronic and optoelectronic devices.

This deliverable presents the main layered 2D materials currently investigated within the PHEMTRONICS project as phase-change materials.

A range of chalcogenides and correlated oxides have been fabricated and characterized for their structural, optical, thermal and electrical properties.
We show experimental demonstrations that thermal and/or light excitation-induced refractive index changes in several of the investigated materials can provide high contrast switching functionality.
Specifically, this deliverable provides an overview of the characterization results achieved within PHEMTRONICS about:

- Group-III Chalcogenides
- Group-V Chalcogenides
- Group-IV Chalcogenides
- Transition Metal Dichalcogenides (TMDs)

Finally, we give an outlook to future opportunities in the study and applications of 2D phase transitions, and identify key challenges that remain to be addressed andphase-change materials to be further optimized within the PHEMTRONICS project.

1. Introduction

When optical phase change materials (O-PCMs) undergo solid-state phase transition, their optical properties are significantly altered. This singular behavior, identified in a handful of chalcogenide alloys exemplified by the Ge–Sb–Te (GST) family,[1] has been exploited in a wide range of photonic devices including optical switches,[2] non-volatile display,[3] reconfigurable meta-optics,[4] tunable emitters and absorbers,[5] photonic memories,[6] and all-optical computers.[7]

To date, these devices only leverage phase change materials originally developed for electronic switching. Optical property modulation in these classical phase change material systems stems from a change in bonding configuration[8] sometime accompanied by a metal-insulator transition (MIT).[9]

Phase change material (PCM) active photonics exploits refractive index switching materials. PCMs are generally characterized by a complex refractive index $N = n + ik$ in both amorphous and crystalline states.

The prototypical phase change material, Ge2Sb2Te5 (GST) can be reversibly switched on a sub-nanosecond time scale billions of times, and once switched no energy is needed to maintain the switched state.[1]

GST is the PCM choice in the infrared and at the telecom wavelength of 1550nm, i.e. for GST, there is a particularly large absorption difference between the two states, with the absorption loss (k = 1.49) in the crystalline phase clearly distinguishable from the amorphous phase (k = 0.12) at telecommunication wavelength. However, even the amorphous phase has strong absorption, severely limiting these devices in size and scalability, while the absorption in the crystalline state constricts their use to amplitude modulators rather than to switches and routers.

However, to tune visible photonics devices, GST is non-ideal due to the high absorption at and above bandgap photon energies and the relatively small change in the real component of the refractive index, (n), at visible frequencies. The small (n) together with using ultrathin GST layers, which are necessary to minimize excessive absorption of the visible light, further restrict the phase transition induced optical path length change at visible wavelength.

Another popular phase-change material is VO_2, due to the fast electrical switching speeds and low transition temperature of 68 °C. The metallic state is volatile at room temperature, which makes it an attractive material for some applications such as modulation and reconfigurable antennas.[10] The optical loss is also an issue for larger photonic circuits with the absorption at 1550 nm in both phases being comparable to GST, with a smaller Δn = 0.5, the absorption (k = 0.5) is still too high for VO_2 to be integrated into photonic circuits that work with phase modulation.[11]

To solve the absorption problem, a new class of O-PCMs PCMs with wider optical bandgaps and with a low optical absorption in the visible spectrum are required to tune photonic structures. For these materials the phase transition only triggers refractive index modulation without the loss penalty.

[1] M. Wuttig, N. Yamada, *Nat. Mater.* **2007**, *6*, 824]

[2] Stegmaier, M., Ríos, C., Bhaskaran, H., Wright, C. D. & Pernice, W. H. Nonvolatile all-optical 1 × 2 switch for chipscale photonic networks. *Adv. Optical Mater.* **5**, 1600346 (2017).

[3] Wang, Q. et al. Optically reconfigurable metasurfaces and photonic devices based on phase change materials. *Nat. Photonics* **10**, 60–65 (2016).

[4] Dong, W. et al. Tunable mid-infrared phase-change metasurface. *Adv. Optical Mater.* **6**, 1701346 (2018).

[5] Tittl, A. et al. A switchable mid-infrared plasmonic perfect absorber with multispectral thermal imaging capability. *Adv. Mater.* **27**, 4597–4603 (2015).

[6] Cheng, Z. et al. Device-level photonic memories and logic applications using phase-change materials. *Adv. Mater.* **30**, 1802435 (2018).

[7] C. Kaspar, B. J. Ravoo, W. G. van der Wiel, S. V. Wegner & W. H. P. Pernice, The rise of intelligent matter. Nature, 594, **345** (2021).

[8] Wuttig, M., Deringer, V. L., Gonze, X., Bichara, C. & Raty, J.-Y. Incipient metals: functional materials with a unique bonding mechanism. *Adv. Mater.* **30**, 1803777 (2018).

[9] Siegrist, T. et al. Disorder-induced localization in crystalline phase-change materials. *Nat. Mater.* **10**, 202 (2011).

[10] B. Gerislioglu, A. Ahmadivand, M. Karabiyik, R. Sinha, N. Pala, *Adv. Electron. Mater.* **2017**, *3*, 1700170]

[11] .C. Wan, Z. Zhang, D. Woolf, C. M. Hessel, J. Rensberg, J. M. Hensley, Y. Xiao, A. Shahsafi, J. Salman, S. Richter, Y. Sun, M. M. Qazilbash, R. Schmidt-Grund, C. Ronning, S. Ramanathan, M. A. Kats, *Ann. Phys.* **2019**, *531*, 1900188.

Potential two-dimensional (2D) van der Waals crystals with mechanical flexibility, transparency, and low cost are viable material platforms for future nanodevices.

PHEMTRONICS aims to introduce new materials that are being developed specifically for tuneable phase change photonics applications and is expanding the PCM space map as shown in Figure 1.

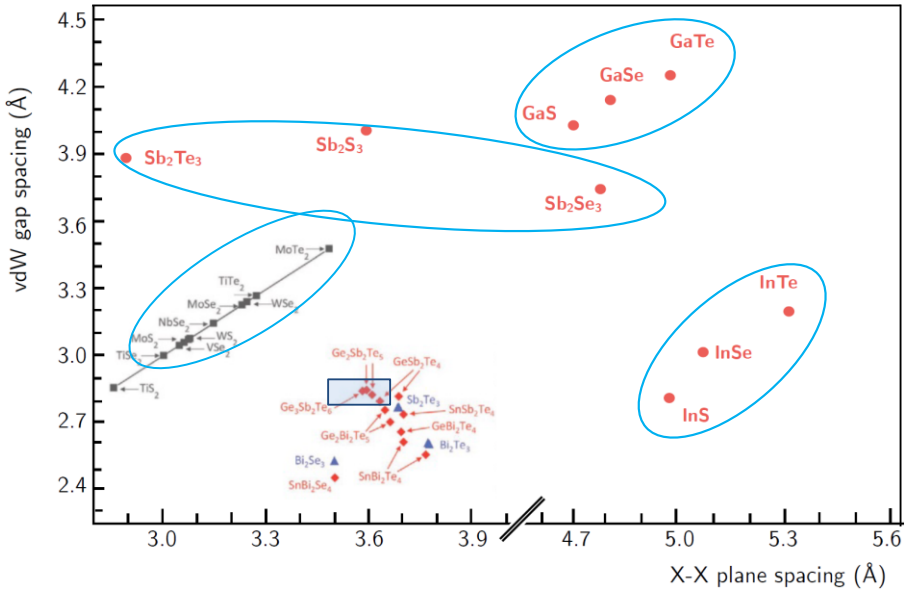

Figure 1: *PHEMTRONICS expansion (blue circles domains) of space map of layered 2D materials considered for phase change*

Coordination-related, two-dimensional (2D) structural phase transitions are a fascinating facet of two-dimensional materials with structural degeneracy.
Very recently, 2D group III–V,[12] II–VI,[13] V–V semiconductors,[14] 2D metal oxides[15] and transition metal dichalcogenides (2D-TMDs) and many other compositionally diverse 2D materials have been predicted and synthesized. III–VI monochalcogenides, where M is a group III element (Ga, In) and X is a chalcogen (S, Se, Te) and V-VI chalcogenides are a relatively unexplored part of the layered semiconductor family.
The discovery and control of new phases of matter is a central endeavour in materials research. The emergence of atomically thin 2D materials, such as the above mentioned dichalcogenides and monochalcogenides, has allowed the study of diffusive, displacive and quantum phase transitions in 2D.
Reduction of dimensionality, i.e., thee trans-dimensional regime that PHEMTRONICS aims at addressing, can strongly affect internal interactions and statistical physics, and, thus, the behavior of phase transitions. Because of the few layer thickness of 2D PCMs, dielectric screening normal to the layer is limited; a 2D material in the out-of-plane direction resembles a molecule surrounded by vacuum. Therefore, the electrostatic potential generated by lattice vibrations in 2D materials is less screened than in 3D bulk materials, which increases the strength of electron–phonon interactions. Consequently, 2D materials are more susceptible to charge density wave and Peierls distortions,[16] lattice instabilities that can considerably alter the short- range coordination and bonding symmetry.
These unique features of 2D phase transitions have led to new concepts for engineering the phases and properties of 2D materials

By adopting layered materials PHEMTRONICS aims at exploring new phase engineering concepts

[12] T. Suzuki, Theoretical discovery of stable structures of group III–V monolayers: the materials for semiconductor devices Appl. Phys. Lett. 107 213105–9 (2015).
[13] H. Zheng et al. Monolayer II–VI semiconductors: a firstprinciples prediction Phys. Rev. B 92 115307–17 (2015).
[14] W. Y. Yu et al. Atomically thin binary V–V compound semiconductor: a first-principles study J. Mater. Chem. C 4 6581–7 (2016).
[15] P. Kumbhakar et al. Emerging 2D metal oxides and their applications. Materials Today, 45, 142-168 (2021)
[16] Xi, X. X. et al. Strongly enhanced charge- density-wave order in monolayer NbSe2. *Nat. Nanotechnol.* **10**, 765–769 (2015)

For example, the possibility of precise spatial addressability (as 2D locating is much easier than 3D locating), strong coupling with light and the propensity for displacive phase transitions enable optomechanical switching. Here, a laser beam is used to induce ultrafast, *diffusionless martensitic non-equilibrium,* order- to-order phase transitions in 2D materials with degenerate ground states,[17]
Figure 2 summarizes the requirement of the new PCMs PHEMTRONICS is pursuing.

CONVENTIONAL PHASE CHANGE APPROACH AND MATERIALS	PHEMTRONICS APPROACH
Amorphous-crystalline phase	Can we design some c**rystalline-to-crystalline** phase transition materials?
Transformation belongs to the **diffusional phase transition**	**Diffusionless** phase transformation displacive/ **martensitic**
Temperature-driven transformation	**Light**-driven atomic displacement can be reduced on the order of unit cell length
All phonon modes are involved, and thus, the **energy** and the heat dissipation are significant	Phase transition preferably occurs within a **single phonon oscillation** period, and thus, would have the benefits of **low energy consumption**, low heat load
The phase change occurs on a timescale of hundred **micro- nanoseconds**	Reduce the phase transition timescale to < **picoseconds**

Figure 2: *Conventional PCMs and approach in red compared to the PHEMTRONICS proposition in blue*

From an engineering perspective, this creates both opportunities and challenges for controlling and using phase change in 2D due to strong light–matter interactions in 2D. Figure 3 summarizes examples of phase transformations that are enabled in 2D materials in addition to the conventional amorphous-crystalline transition exploited by GST.
The 2D materials chalcogenides exhibit polymorphic phase transitions in near- ambient conditions because chalcogen elements (S, Se and Te) have a relatively small electronegativity and, thus, in many chalcogenides, ionic and covalent bonding compete, which leads to the generation of structural polymorphs with different bonding configurations that are close in energy. Therefore, perturbations induced by weak external stimuli can drive polymorphic transitions in these materials. Examples of those enabled polymorph transitions include the metal-insulator 2H->1T phase in MoS_2 and $MoTe_2$,[18] the order-order transformation between two crystalline phases (e.g. orthorhombic→monoclinic) and ferroelastic transitions (e.g. in group-IV chalcogenides).
However, air stability, chemical purity become bigger issues in 2D and influence the phase- change behavior. This makes very challenging identifying and fabricating 2D PCMs and their assessment requires extensive characterization.

This deliverable experimentally considers various classes of 2D materials with potential for phase transformation as those listed in Fig.1, namely:

- Group-III Chalcogenides (InS, InSe, GaS, Ga_2S_3, GaSe, GaTe)
- Group-V Chalcogenides (Sb_2S_3)
- Group-IV Chalcogenides (GeS, GeSe)
- Transition Metal Dichalcogenides (TMDs) (MoS_2, MoO_x)

It reports the extensive characterization performed on several PCMs from the above groups aimed at identifying candidates of phase-change materials for applications in phase-change photonics.

[17] Zhou, J., Xu, H. W., Li, Y. F., Jaramillo, R. & Li, J. Opto- mechanics driven fast martensitic transition in two- dimensional materials. *Nano Lett.* **18**, 7794–7800 (2018).
[18] Duerloo, K.-A. N., Li, Y. & Reed, E. J. Structural phase transitions in two- dimensional Mo- and W- dichalcogenide monolayers. *Nat. Commun.* **5**, 4214 (2014).
This paper reports the first comprehensive theoretical study of structural phase transitions in monolayer transition- metal dichalcogenides

- Crystalline ↔ amorphous
- Metal ↔ insulator : 2H ↔ 1T
- Layered ↔ Hexagonal
- Ferroelastic domain

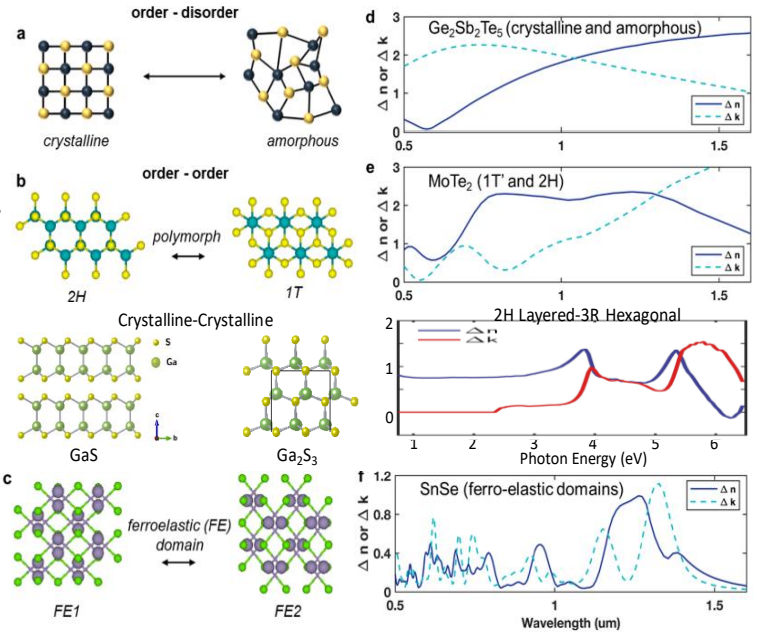

Figure 3: *Types of phase transformation considered in PHEMTRONICS by trans-dimensional materials*

2. Synthesis Methodologies in Phemtronics

Several synthesis approaches compatible wwith device fabrication are being explored within PHEMTRONICS project, considering that the characteristics of the obtained materials strongly depends on the approach.

	Mechanical exfoliation	Chemical vapour deposition (CVD)	Plasma Enhanced Chemical Vapor Deposition (PECVD)	Atomic Layer Deposition (ALD)	Sputtering/ Evaporation	Chemical Bath Deposition (CBD)
CNR	👍	👍	👍			
UCC-Tyndall				👍	👍	
NANOM	👍					👍

3. Synthesized Materials Characterization

The table below summarizes the approaches used to characterize the synthetized PCMs.

Chemical/composition	X-ray photoelectron spectroscopy (XPS)	Energy x-ray dispersion spectroscopy (EDX)	Infrared Spectroscopy (FTIR)	
Structural	X-ray diffraction (XRD)	Transmission electron Microscopy (TEM)	Scanning Electron Microscopy (SEM)	Raman Spectroscopy
Morphology	Atomic Force Microscopy (AFM)	Kelvin probe Microscopy	Lateral Force Phase scanning microscopy	
Optical Properties	Spectroscopic Ellipsometry	Transmission/ Reflection	Imaging Polarimetry	Photoluminescence
Electrical properties	Hall Effect	I-V characteristics	Photoconductivity	

Considerable efforts both theoretically and experimentally are dedicated to establishing the dielectric function of those novel PCMs both at bulk and monolayer level.
First, we determined the bulk dielectric function of the layered materials under investigation, using certified crystals. Then, we determine the dependence of layered chalcogenides PCMs as a function of the thicknesses and/or number of layers. Additionally, on the grown amorphous materials, we have determined the dielectric function as a function of the growth condition to establish the range of possible dielectric function spectra of amorphous phases, as in the amorphous case the dielectric function may be deposition condition and structure dependent (grade of order/disorder as well as stoichiometry and defects). We are establishing a database of optical constants, refractive index (*n*), and extinction ratio (*k*), for crystalline and amorphous PCMs, as *n* and *k* are the key parameters for optical applications as a function of thickness.

4. Developed Colorimetric Approach for Thickness Determination of layered Materials

We have developed within PHEMTRONICS a colorimetric reflectometry method[19] based on optical microscopy to quickly and reliably infer the thickness of flakes of 2D materials, providing guidelines for the accurate and systematic colorimetric assessment of the thickness determination of low dimensional materials on several substrate that are often used for different technological applications. An example, of how layers of different number/thickness appear colored at an optical microscope is given in Figure 4.

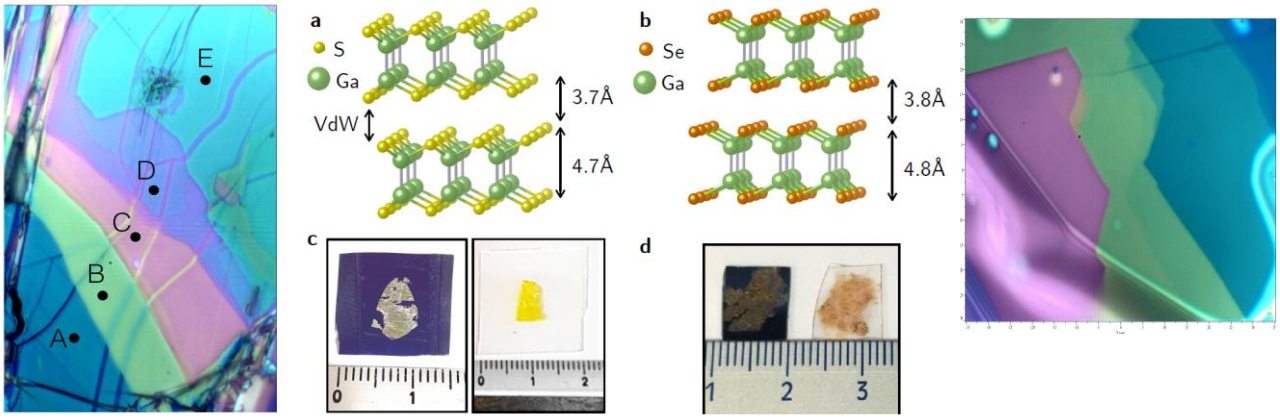

Figure 4: *(Left and Right) optical micrographs of various layers of GaS and GaSe transferred on glass.*

Our method, summarized in Figure 5, is based on the optical constants we determine by spectroscopic ellipsometry within the PHEMTRONICS consortium used to simulate the spectral reflectance of 2D PCMs layers of different thicknesses on various substrates, using the transfer matrix method and its transformation to color coordinates using color matching functions. The simulated color for each thickness has been validated by the comparison with the real color observed by an optical microscope of GaS flakes whose thickness is determined by atomic force microscopy (AFM).

[19] Y. Gutierrez et al. Appl. Phys. Lett. Submitted (2021)

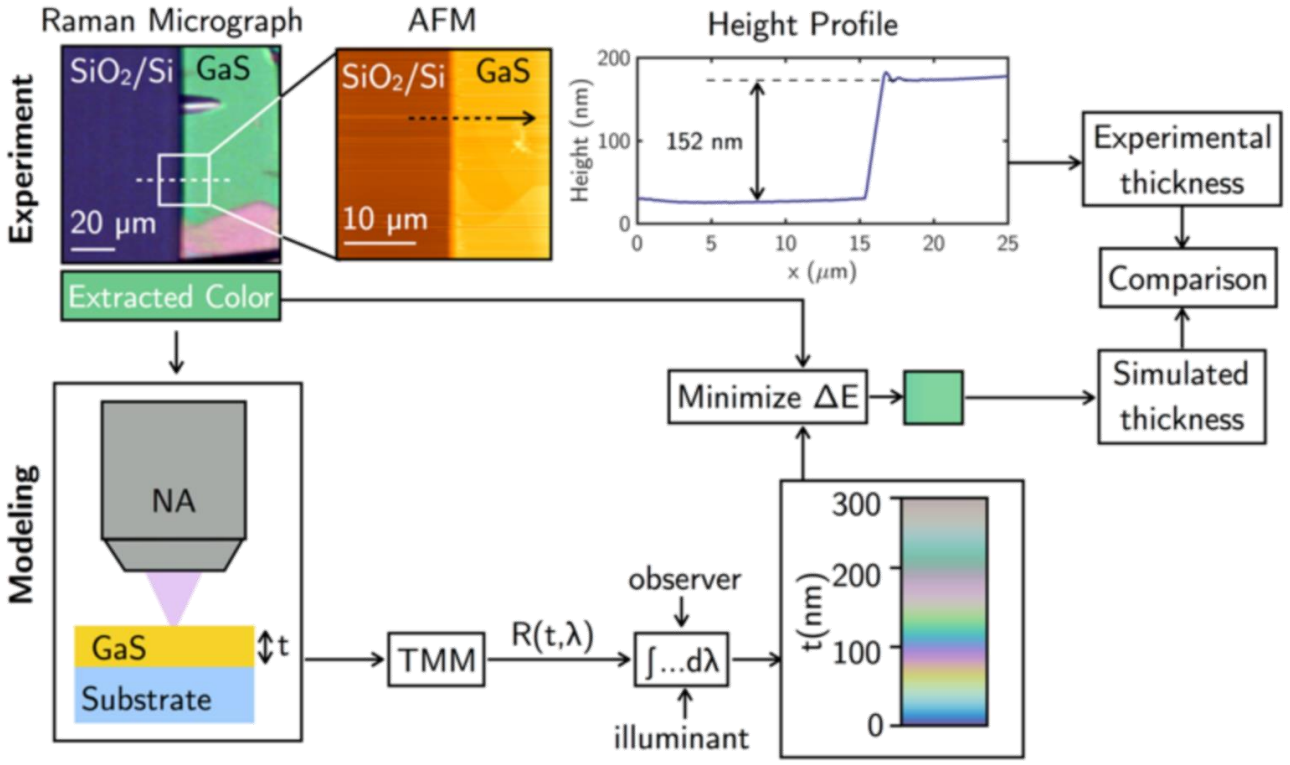

Figure 5: *Flow diagram of the model evaluation for the developed colorimetric approach to thickness determination of layered PCMs.*

Generalized colors palettes, called Color-Thickness Rulers" have been established for several PCMs. Here, we show in Figure 6 an example for GaS and GaSe on various technological substrates are provided that can be used by anyone taking optical micrographs of exfoliated GaS and GaSe as a quick guide for the rapid and reliable thickness determination of GaS and GaSe layers on those substrates.
The proposed generalized optical identification model and color palettes will facilitate the thickness dependent investigation of 2D semiconductors, expediting their practical applications.
This approach is a running publication of PHEMTRONICS and will be soon available as exploitable code on the PHEMTRONICS website.

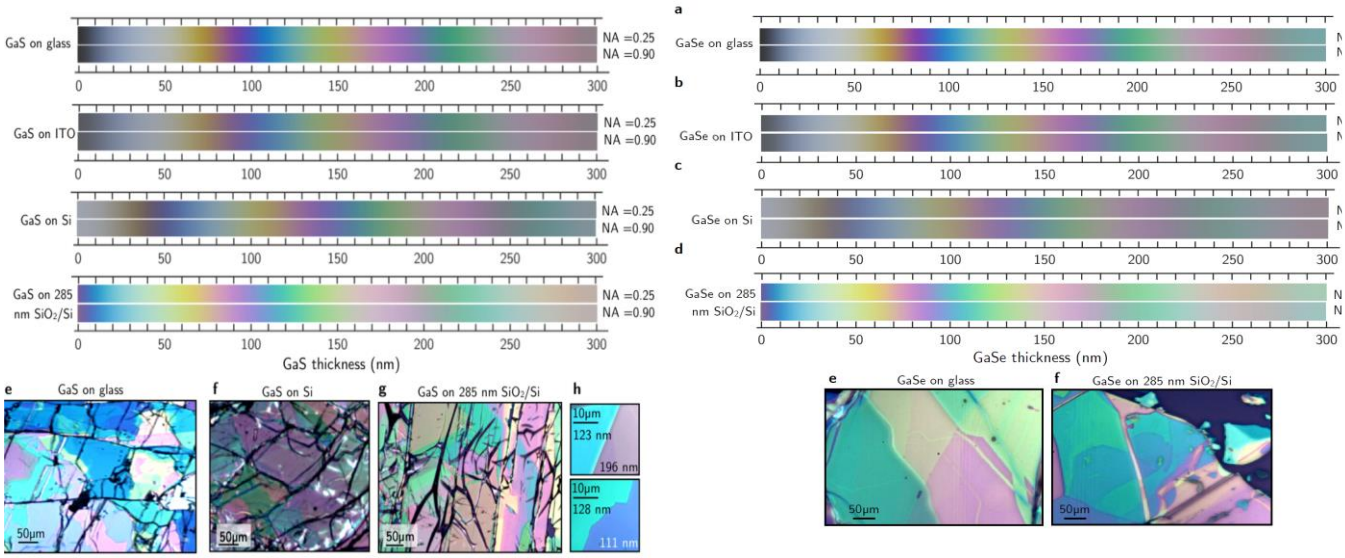

Figure 6*: Color evolution of GaS and GaSe layers on different substrates as a function of their thickness. Micrograph pictures are also given to show the color appearance in real samples. In (h) the smaller micrographs show homogenous regions with their predicted thickness.*

5. Overview of Group-III Chalcogenides

Group-III, Indium (In) and Gallium (Ga) chalcogenides have a broad spectrum of polymorphic crystallographic phases. This applies to sulphides, selenides and tellurides series InS, InSe, InTe as well as to GaS, GaSe and GaTe. An example of this can be seen in the indium sulphide series, where InS, In_3S_4, In_6S_7 and In_2S_3 (α-In_2S_3, β- In_2S_3, and γ- In_2S_3) have been deposited experimentally by CVD and similarly for the indium selenides. Also Indium telluride, InTe, is not very common since it easily tends to separate indium and tellurium.
The properties of some of the obtained phases are reported in Table I.
All those indium materials indeed, synthetized by CVD showed problem of instability and of control of stoichiometry, being easily indium rich and prone to oxidation to In_2O_3, while separating elemental sulphur, selenium and tellurium; therefore, their phases could not be controlled under annealing and/or light irradiation.

Because of the tendency of indium to oxidize to In_2O_3, a decision has been made not to further explore indium-chalcogenides as PCMs.

Table I: *Selected Indium-Chalcogenides phases and main properties*

Compound	Structural type	Crystallographic system	Cell parameters (Å, °)	Band gap (eV)[a]
β-InS	GaS	Orthorhombic	a = 3.944, b = 4.447, c = 10.648	2.58 (dir.), 2.067 (ind.)
InS[b]	Hg_2Cl_2	Tetragonal		
InSe	GaS	Rhombohedral	a = 4.00, c = 25.32	1.3525 (dir.), 1.32 (ind.)
β-InSe	GaS	Hexagonal	a = 4.05, c = 16.93	
InTe	TlSe	Tetragonal	a = 8.437, c = 7.139	Metallic
InTe[b]	NaCl	Cubic	a = 6.18	
α-In_2S_3	γ-Al_2O_3	Cubic	a = 5.36	
β-In_2S_3	Spinel	Tetragonal	a = 7.618, c = 32.33	2.03 (dir.), 1.1 (ind.)
α-In_2Se_3	Defect wurtzite	Hexagonal	a = 16.00, c = 19.24	
β-In_2Se_3	Defect wurtzite	Rhombohedral	a = 4.025, c = 19.222	1.2 - 1.5 (ind.)
α-In_2Te_3	Sphalerite	Cubic	a = 6.158	0.92 - 1.15 (opt.)
In_6S_7		Monoclinic	a = 9.090, b = 3.887, c = 17.705, β = 108.20	0.89 (dir.), 0.7 (ind.)
In_6Se_7	In_6S_7	Monoclinic	a = 9.430, b = 4.063, c = 18.378, β = 109.34	0.86 (dir.), 0.34 (ind.)
In_4Se_3		Orthorhombic	a = 15.297, b = 12.308, c = 4.081	0.64 (dir.)
In_4Te_3	In_4Se_3	Orthorhombic	a = 15.630, b = 12.756, c = 4.441	0.48 (dir.)

Differently from indium-chalcogenides, gallium-chalcogenides of gallium sulfide (GaS), gallium selenide (GaSe) and gallium telluride (GaTe) are much more stable, especially GaS and are also characterized by polymorphism as shown in Table II, where the main properties of the various phases have been indicated.
Materials in this group are mostly hexagonal, with the exception of Te-based compounds which crystallize in a lower symmetry monoclinic form

Thin films of GaS, GaSe and GaTe have been synthetized in PHEMTRONICS by mechanical exfoliation, chemical vapor deposition (CVD) and atomic layer deposition (ALD) on various substrates of glass, c-axis oriented sapphire, SiO_2/Si substrates and Si_3N_4/SiO_2/Si waveguides and their main characteristics that are guiding the PHEMTRONICS consortium in the selection of those materials most promising as PCMs are reported in the following paragraphs.

Table II: *Selected Gallium-Chalcogenides phases and main properties*

Compound	Structural type	Crystallographic system	Cell parameters (Å, °)	Band Gap (eV)[a]
GaS		Hexagonal	a = 3.587, c = 15.492	3.05 (dir.), 2.593 (ind.)
GaS	ZnS or NaCl	Cubic	a = 5.5	4.0 (opt.)
β-GaSe	GaS	Hexagonal	a = 3.742, c = 15.919	2.103 (dir.), 2.127 (ind.)
γ-GaSe	GaS	Rhombohedral	a = 3.755, c = 23.92	
δ-GaSe	GaS	Hexagonal	a = 3.755, c = 31.99	
β-GaTe	GaS	Hexagonal	a = 4.06, c = 16.96	
GaTe	GaS	Monoclinic	a = 17.44, b = 4.077, c = 10.456, β = 104.4	1.799 (dir.)
α-Ga_2S_3	Wurtzite	Cubic	a = 5.181	
α-Ga_2S_3	Wurtzite	Monoclinic	a = 12.637, b = 6.41, c = 7.03, β = 131.08	3.438 (opt.)
β-Ga_2S_3	Defect wurtzite	Hexagonal	a = 3.685, c = 6.028	2.5 - 2.7 (opt.)
α-Ga_2Se_3	Sphalerite	Cubic	a = 5.429	2.1 (dir.), 2.04 (ind.)
α-Ga_2Te_3	Sphalerite	Cubic	a = 5.886	1.22 (opt.)

5.1 Characterization of thick crystalline films of GaS, GaSe and GaTe

We started by depositing thick films in order to establish the bulk reference fundamental properties, which were not known.

GaS, GaSe and GaTe thin films with thicknesses of ≈ 1µm as estimated from ellipsometric measurements have been deposited on sapphire as shown in Figure 7 and have been structurally and optically studied both in their pristine state as well as after one week of air exposure. Already the picture of those samples shows visibly the fast degradation of GaTe, which also delaminate by air exposure and in time due to tellurium (Te) segregation as shown in the below.

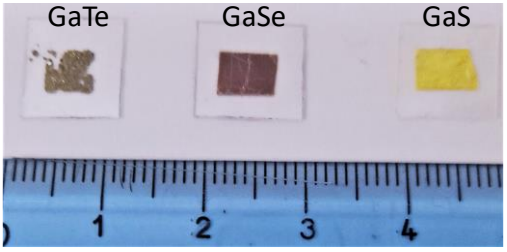

Figure 7: *Picture of layered thick (>100nm) samples of GaTe, GaSe and GaS deposited on sapphire.*

XRD analysis of all the crystalline (and microcrystalline) samples showed that they are highly (0001) oriented with 105 and 107 edges, as indicated by typical XRD diffraction patterns shown in Figure 8 for GaS.

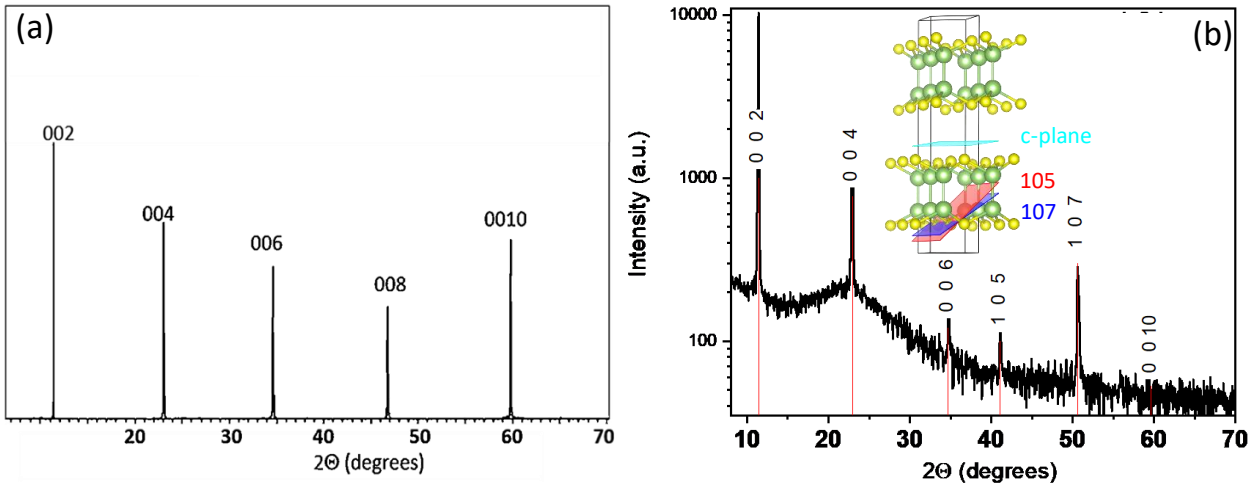

Figure 8: *Typical XRD patters recorded for crystalline (a) and microcrystalline (b) samples of GaS.*

The GaS thin film shows a uniform flat surface as revealed by the micrograph and AFM topography phase images shown in Figure 9a. The real and imaginary parts of the pseudodielectric function measured on the pristine sample and after one week of air exposure are shown in Figure 9b. The imaginary part of the pseudodielectric function is consistent with values found in literature, showing two sharp peaks consistent with the GS2 and S3 critical points of GaS.[20] The spectra for the pristine sample and before air exposure are coincident, revealing the good ambient stability of GaS. Raman spectra were also taken on the pristine sample and after one week of air exposure. The Raman spectra of GaS is characterized by three peaks, which are unaltered by the exposure of GaS to air, at 185, 291 and 357 cm^{-1} assigned to the $\boldsymbol{A_{1g}^1}$, $\boldsymbol{E_{2g}^1}$ and $\boldsymbol{A_{1g}^2}$ Raman modes as shown in Figure 9c.

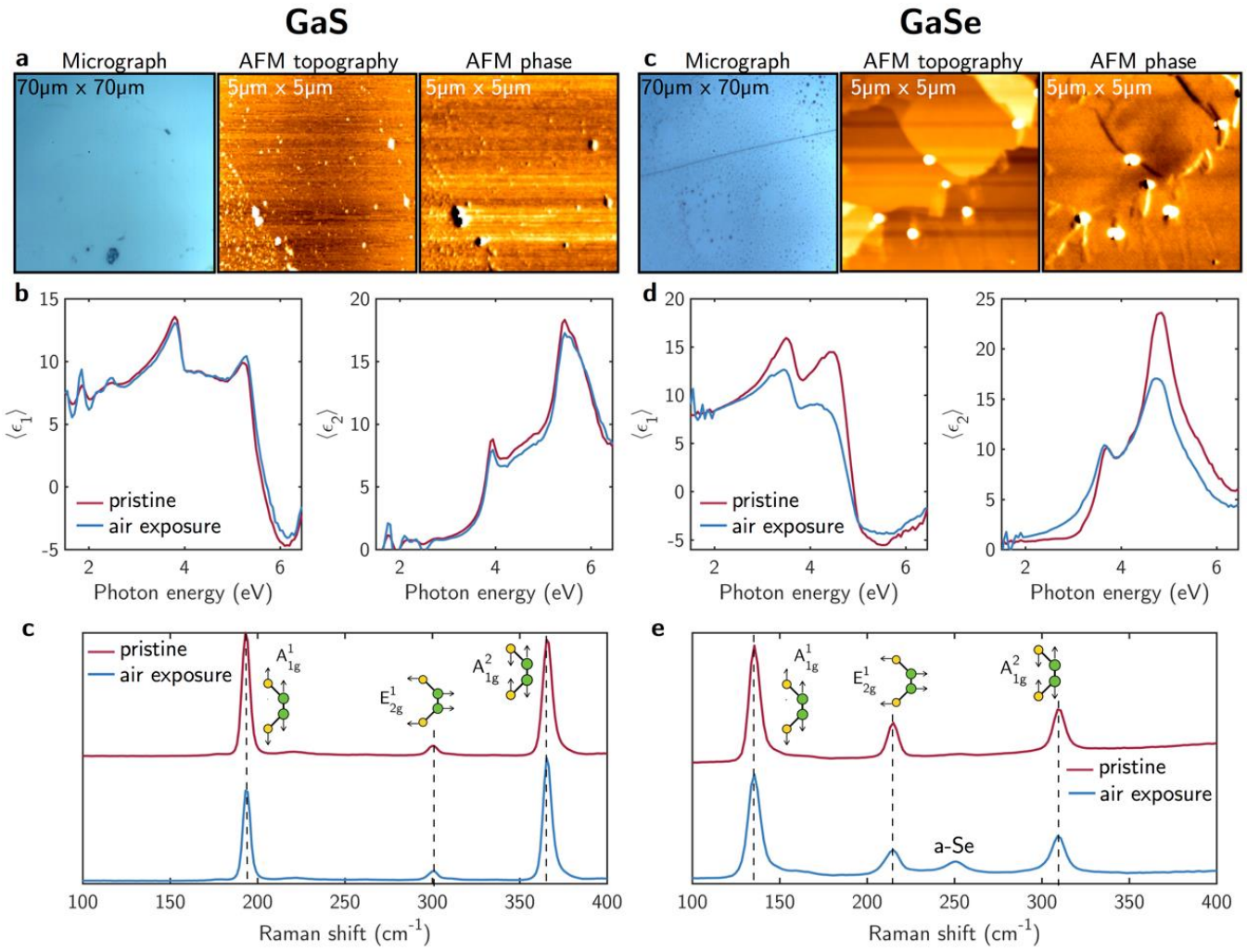

Figure 9. *Micrographs and AFM topography and phase of (a) GaS and (b) GaSe thinfilms. (b,d) Pseudodielectric function and (c,e) Raman spectra of (b,c) GaS and (d,e) GaSe thinfilms. All the spectra were recorded in pristine samples (red lines) and after one week of air exposure (blue lines).*

[20] Isik, M., Gasanly, N. M. & Turan, R. Interband transitions in gallium sulfide layered single crystals by ellipsometry measurements. *Phys. B Condens. Matter* 408, 43–45 (2013)

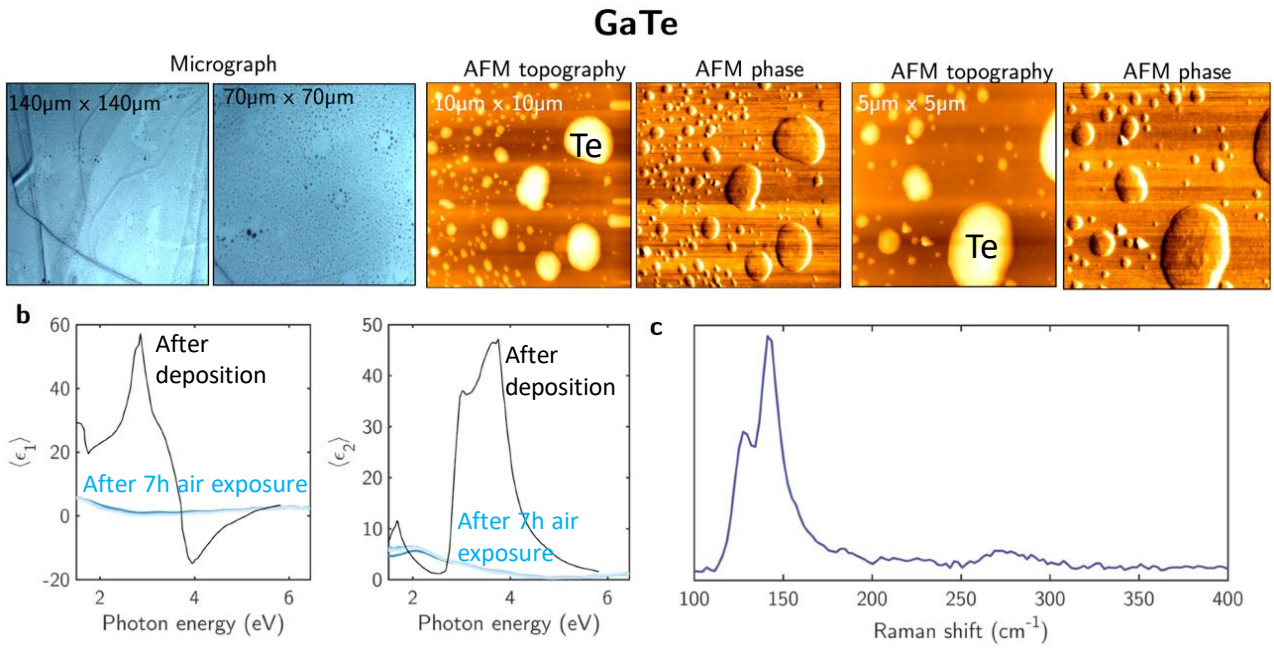

***Figure 10**: (a) Micrograph and AFM topography and phase images of the surface film. (b) Pseudodielectric function and (c) Raman spectrum of GaTe films.*

Parallel experiments were carried out on a GaSe thin film. Similarly to GaS, the micrograph of the pristine GaSe sample showed a flat surface; however, differently from GaS, after one week of air exposure GaSe was covered by a granular red texturing as shown in Figure 9c. Further topography and phase AFM analysis and compositional analysis by EDX of the sample revealed the presence of spherical particles of submicron size of a different composition, which was revealed to be Selenium (Se). Figure 9d shows the pseudodielectric function of GaSe before and after air exposure. The ellipsometric spectra of the pristine sample shows good agreement with that reported in literature showing two main critical points.[21] After one week of air exposure, a broadening and quenching of the two main critical points was also observed. This behavior is consistent with a roughening of the thin film surface produced by the appearance of the submicron particles observed in the AFM images. The Raman analysis of the sample revealed the appearance of a new Raman mode after one-week air exposure as shown in Figure 8e. The spectrum on the pristine sample presents three peaks at 136, 215 and 310 cm^{-1} assigned to the A_{1g}^1, E_{2g}^1 and A_{1g}^2 Raman modes. After one week of air exposure an additional peak at 251 cm^{-1} can be observed compatible with amorphous selenium (a-Se). The presence of a-Se on the Raman spectra may be correlated to the appearance of the submicron particles on the surface of the film. The degradation and appearance of a-Se was also confirmed by chemical analysis of XPS.

Conversely, very rapid degradation upon air exposure was observed for the GaTe film, which completely oxidized. Micrographs and AFM topography and phase images in Figure 10a shows the formation of micron size clusters on the surface of the film that EDX revealed to be Tellurium (Te), attributed to the segregation of Te upon air exposure. This Te segregation also causes delamination of the film as shown in Fig. 7. The ellipsometric and Raman spectra of the GaTe films are shown in Figures 10b,c. The observed Raman bands at 126, 141 and 265 cm^{-1} can be assigned to the hexagonal phase of Te,[22] supporting the Te segregation process consistent with the micrographs and AFM images. Figure 10b shows the pseudodielectric function of the GaTe film compared to that of bulk GaTe dielectric function.[23] The complete quenching of the critical points of the GaTe dielectric function further support the complete oxidation of the GaTe film.

[21] Choi, S. G., Levi, D. H., Martinez-Tomas, C. & Muoz Sanjoś, V. Above-bandgap ordinary optical properties of GaSe single crystal. *J. Appl. Phys.* 106, 1–5 (2009).
[22] Ma, C., Yan, J., Huang, Y., Wang, C. & Yang, G. The optical duality of tellurium nanoparticles for broadband solar energy harvesting and efficient photothermal conversion. *Sci. Adv.* 4, eaas9894 (2018).
[23] Grasso, V., Mondio, G. & Saitta, G. Optical properties of the layer compound GaTe. *Phys. Lett. A* 46, 95–96 (1973).

The origin of the Raman modes at 126 and 141 cm^{-1} is still the subject of some controversy. Some previous first-principles calculations have suggested that these modes can be attributed to first or second-order Raman-active phonon modes, whereas other groups have claimed that they appear only as the products of the GaTe oxidation process. In the latter case, the similarities to both TeO_2 and aged Raman spectra of other Te-containing compounds have been noted, supporting the idea that those peaks result from the oxidation of Te atoms. Here, we attribute these peaks to degradation products because they are consistent with all the other EDX, XPS, AFM and ellipsometry characterizations.
For both In- and Ga- telluride we have evidences supporting that Tellurium-based layered compounds degrade via a complex oxidation reaction. O_2 and/or humidity (water) intercalates between the layers debonding them and forming bonds with highly reactive Te atoms, leading to a structural transition to an oxide phase,

Thus, layered GaTe undergoes a rapid structural transition to a degraded phase in ambient conditions, limiting its utility in devices such as optical switches. Progress in GaTe-based devices will be hindered by poor environmental stability and therefore, it has been decided not to proceed with binary III-tellurides.

5.2. GaS and GaSe Crystalline layers from Monolayer to 100 Layers by Mechanical Exfoliation

In order to determine the reference properties of crystalline layered GaS and GaSe from bulk down to monolayer, samples of GaS and GaSe of different layers have been obtained by mechanical exfoliation of bulk GaS and GaSe crystals, as shown in Figure 11.

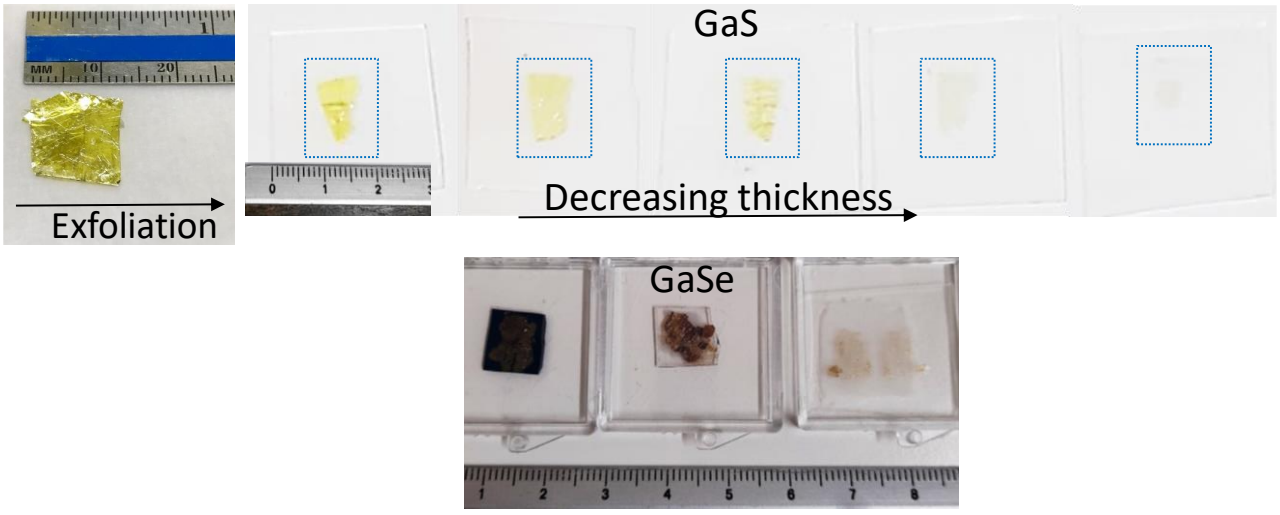

Figure 11: *Mechanical exfoliated samples of GaS and GaSe with decreasing number of layers*

The layered structure is clearly shown by the SEM images in Figure 12. The zoom of the border allows to clearly see the various layers piled-up. The exfoliated GaS layers, even the monolayer, show outstanding stability to air exposure as shown by the reproducibility of the pseudodielectric function and Raman spectra measured before and after a week of air exposure as shown in Figure 12.

All the characterizations support the high stability also of the GaS monolayer in air.

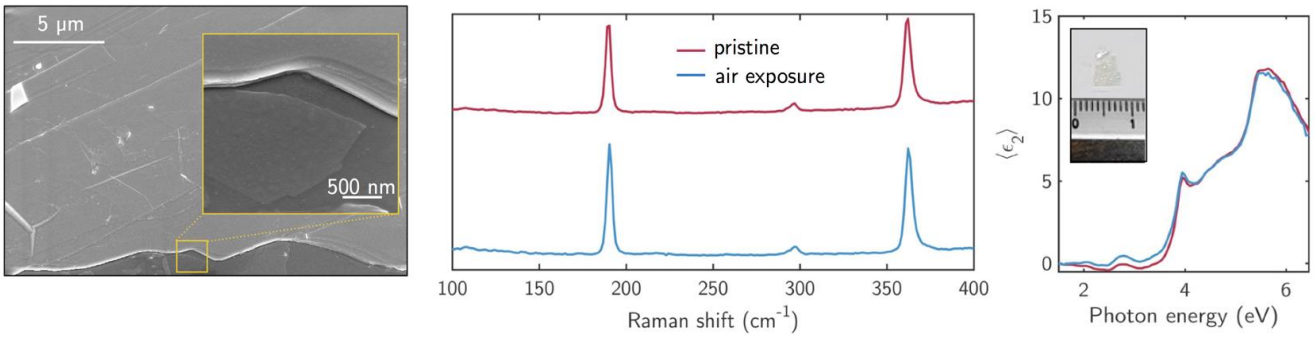

Figure 12. *SEM picture, Raman spectra and pseudodielectric function of ultrathin exfoliated GaS. All the spectra were recorded in pristine samples (red lines) and after one week of air exposure (blue lines).*

The crystalline GaS show all three Raman modes where A^1_{1g} is centered at 188 cm^{-1}, A^2_{1g} is centered at 360 cm^{-1}, and E^1_{2g} is centered at 294 cm^{-1}. Noteworthy, for a high crystalline quality GaS the ratio between the two Raman A_{1g} out-of-plane modes is almost equal to 1.
Since the thickness of the crystalline GaS decreases to the monolayer domains, the frequency of the E^1_{2g} mode increases slightly and the A^1_{1g} mode decreases. Also, the overall intensity decreases as well as shown in Figure 13 for a number of crystalline layers between 1 and 6 layers. Similarly, the optical constants, indicating that thickness of the GaS must also be considered in rationalizing the optical contrast achievable during a phase transformation depending on thickness of the PCM.

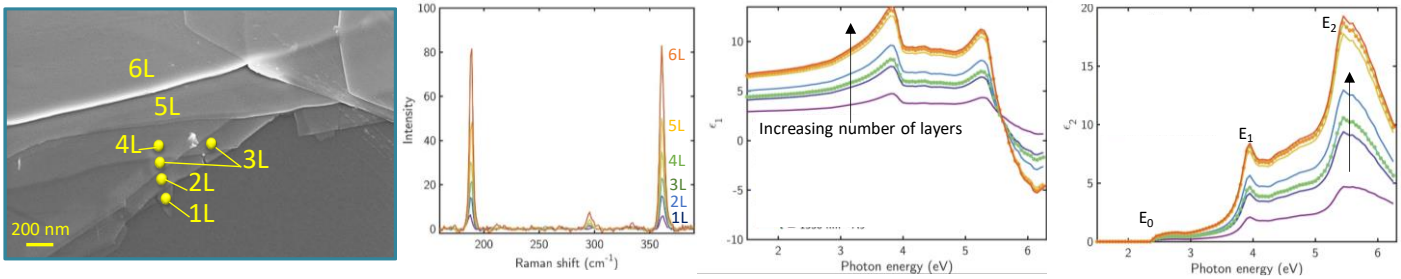

Figure 13: *SEM image of few layers crystalline GaS with corresponding Raman spectra and optical spectra of the real and imaginary part of the dielectric function.*

Those crystalline and stable layers have been used to determine the dielectric function of GaS, which was not known with accuracy., as shown in Figure 14, by the comparison of our determined dielectric function with those previously reported in literature.

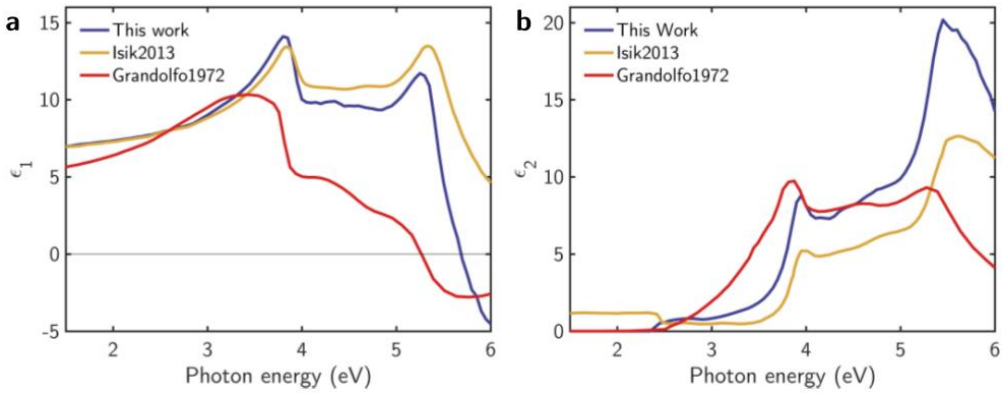

Figure 14*. Experimentally measured complex dielectric function ($\epsilon(\omega) = \epsilon_1(\omega) + i\epsilon_2(\omega)$) of bulk GaS as compared to those values available in the literature.*

Since the accuracy of our data, PHEMTRONICS is developing a database of GaS and GaSe dielectric function and refractive index as a function of number of layers

As for GaSe, Figures 15a,b show that after a week of air exposure, the GaSe surface is completely covered by clusters. The AFM topography and phase images in Figure 15b put in evidence the presence of a high number of submicron spherical particles. The SEM picture clearly reveals the layered structure of the exfoliated GaSe covered by spherical clusters. As shown in Figure 15c, the pseudodielectric function upon air exposure completely changed and damped, not showing any of the critical points characteristics of GaSe pointing out a GaSe degradation process. The structural analysis performed through Raman spectroscopy shows how after air exposure the A_{1g}^1, E_{2g}^1 and A_{1g}^2 Raman modes at 136, 215 and 310 cm^{-1} of GaSe present in the pristine samples are completely quenched after air exposure. Only a small contribution of the A_{1g}^1 mode can be observed. After air exposure the Raman spectrum is dominated by a main peak at 227 cm^{-1} compatible with trigonal Se (t-Se) and with a small contribution of a component at ≈ 250 cm^{-1} (a-Se).
Therefore, GaSe exfoliated ultrathin layers degrade more aggressively than GaSe films due to its higher surface-to-volume ratio.

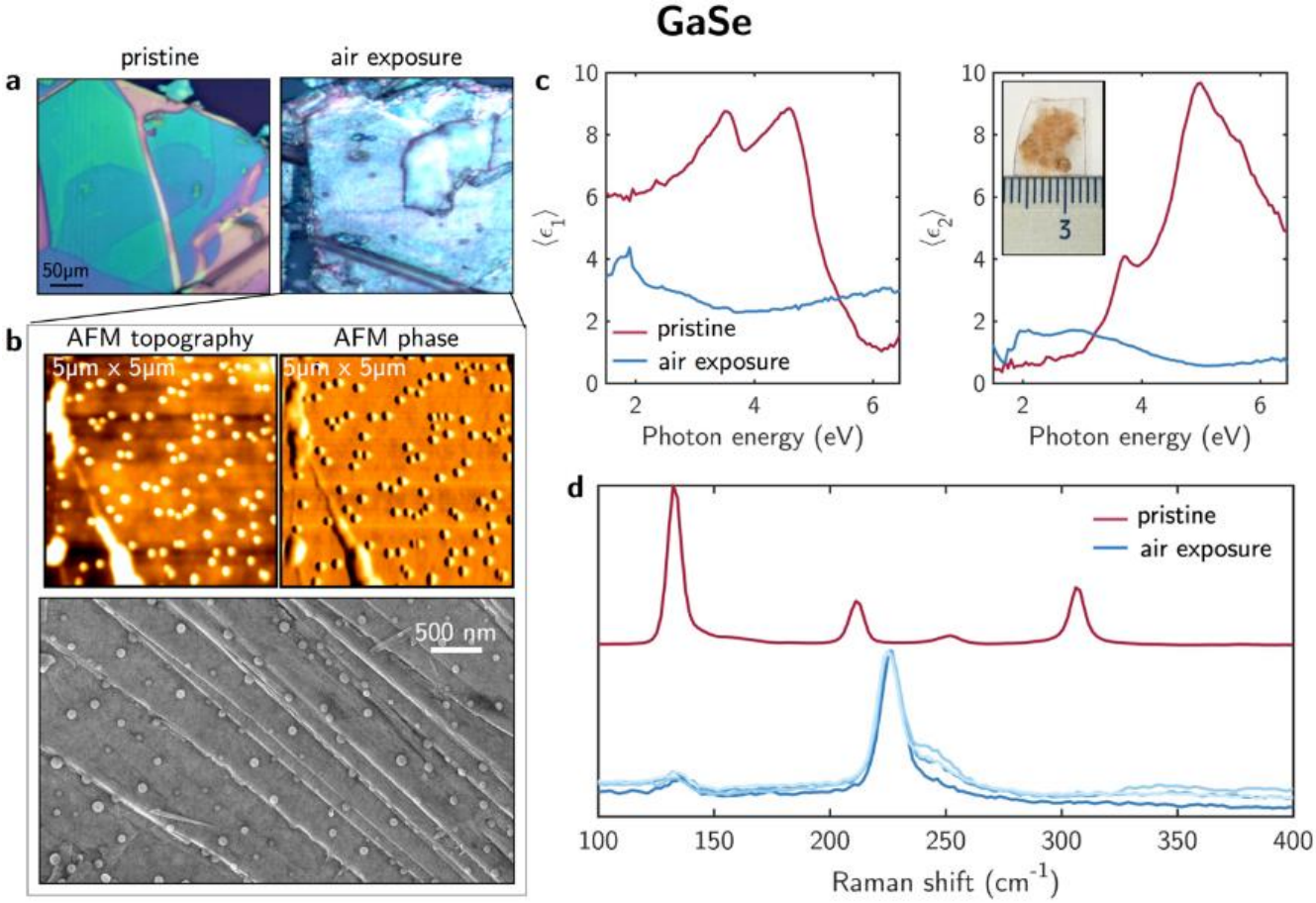

***Figure 15**: Micrographs, AFM and SEM of ultrathin exfoliated GaSe before and after air exposure. (c) Pseudodielectric function and (d) Raman spectra of ultrathin exfoliated GaSe. All the spectra were recorded in pristine samples (red lines) and after one week of air exposure (blue lines). As inset in (c) is shown a picture of the analyzed sample.*

GaSe is stable as bulk, but its surface is unstable. This implies that decreasing the thickness and going down to few layer the degradation/oxidation process increases.
Any use of GaSe in electro-optical devices requires processing of stabilization of GaSe.
PHEMTRONICS has identified two ways: encapsulation of GaSe, e.g. by graphene, or alloying GaSe.

5.3. GaS as Phase Change Material candidate

Crystalline and amorphous GaS layers have been synthetized by low pressure CVD on glass, sapphire and Si/SiO_2 substrates using Ga_2S_3 powder as precursor and H_2/Ar/He as carrier gas. The composition and structure of CVD GaS strongly depend on the growth temperature, carrier gas flow and pressure. The XPS analysis highlighted the possibility of depositing GaS via CVD and the possibility of tuning its chemical composition by acting on the temperature and reducing atmosphere of the carrier gas during the growth. Figure 16 shows the typical survey XPS spectra of a CVD grown crystalline GaS samples, indicating mainly photoelectron core levels from Ga and S; no other impurities are induced by the growth process, apart adventitious adsorbed C-from air exposure and oxygen, forming Ga_2O_3 native oxide as shown in Figure 17.

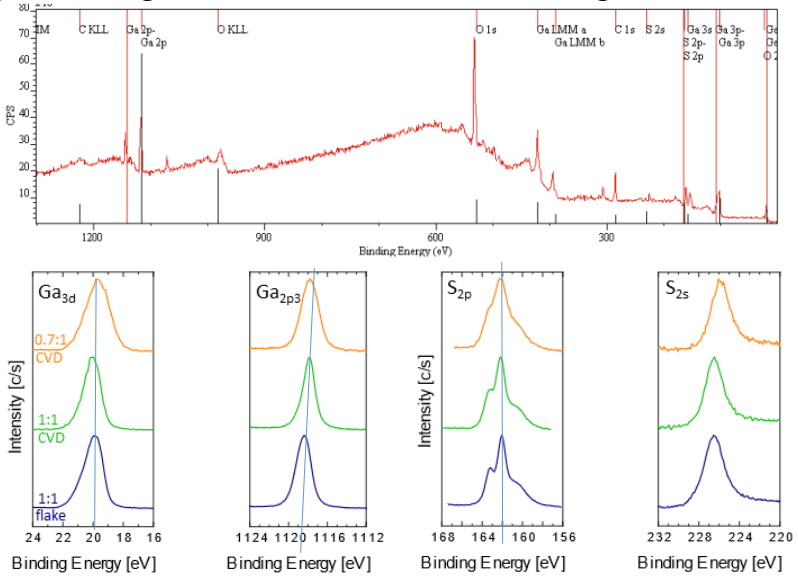

Figure 16. *Survey spectrum of a typical CVD GaS sample. High resolution (HR) XPS spectra of the Ga3d, Ga2p$_{3/2}$, S2p, and S2s for the CVD GaS deposited in pure pure H_2 (top curve) and He (mid curve) and a single crystal GaS (bottom curve). The S:Ga ratio calculated from the elemental analysis taking into account the Ga2p$_{3/2}$ and S2s are also reported.*

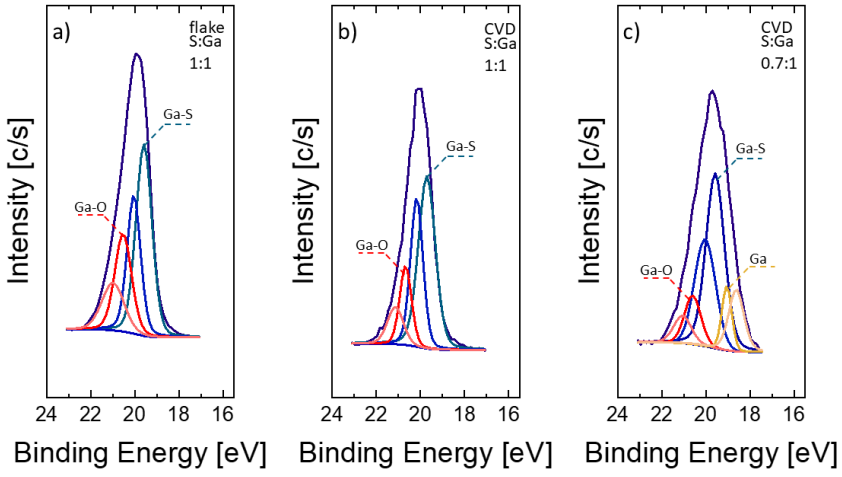

Figure 17*: Best fitting performed on the HR Ga3d spectra of a) commercial single crystal GaS flake, b) CVD GaS in pure He, c) CVD GaS in pure H_2.*

From the elemental analysis, the single crystal resulted in a S:Ga ratio of 1.00 ± 0.02, as expected. The CVD layer deposited in pure He and/or Ar showed a S:Ga ratio of 0.98 ± 0.02, leading to stoichiometric layers, whereas H_2 as carrier gas, introduces the possibility to have Ga-rich GaS layers, leading to different optical, electrical and photoluminescence properties analyzed to understand the response to various stimuli during phase transformation.

Figure 18 shows pictures of samples of various structure.

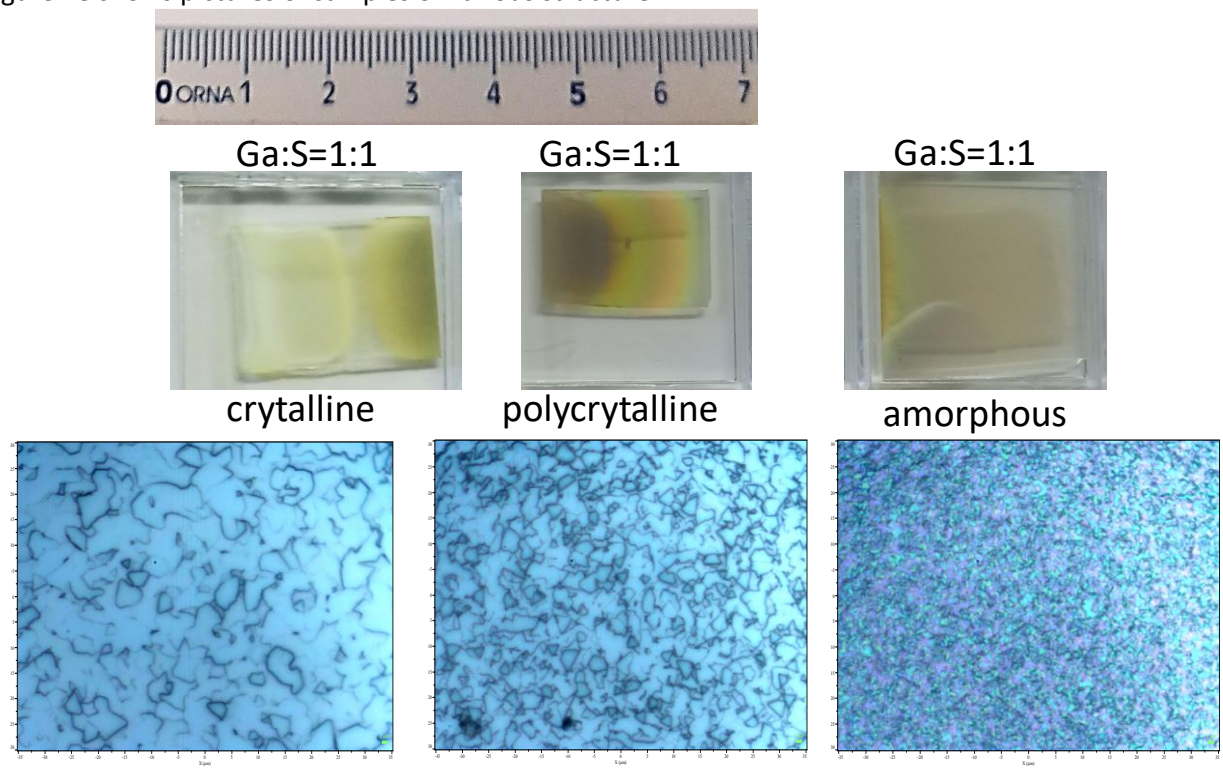

Figure 18: *Pictures and 70μm x70μm optical micrographs of GaS crystalline, polycrystalline and amorphous samples. The optical micrograph of the crystalline sample shows the coalescence of the typical hexagonal and triangular GaS crystallites to form a complete layer.*

The crystalline structure of the CVD amorphous and crystalline samples has been confirmed by XRD analysis shown in Figure 19 for two typical samples. Noteworthy, the highly oriented c-axis (0001) orientation of the deposited CVD crystalline sample. The layered structures can be also seen from the AFM topography of the crystalline grain reported as inset.

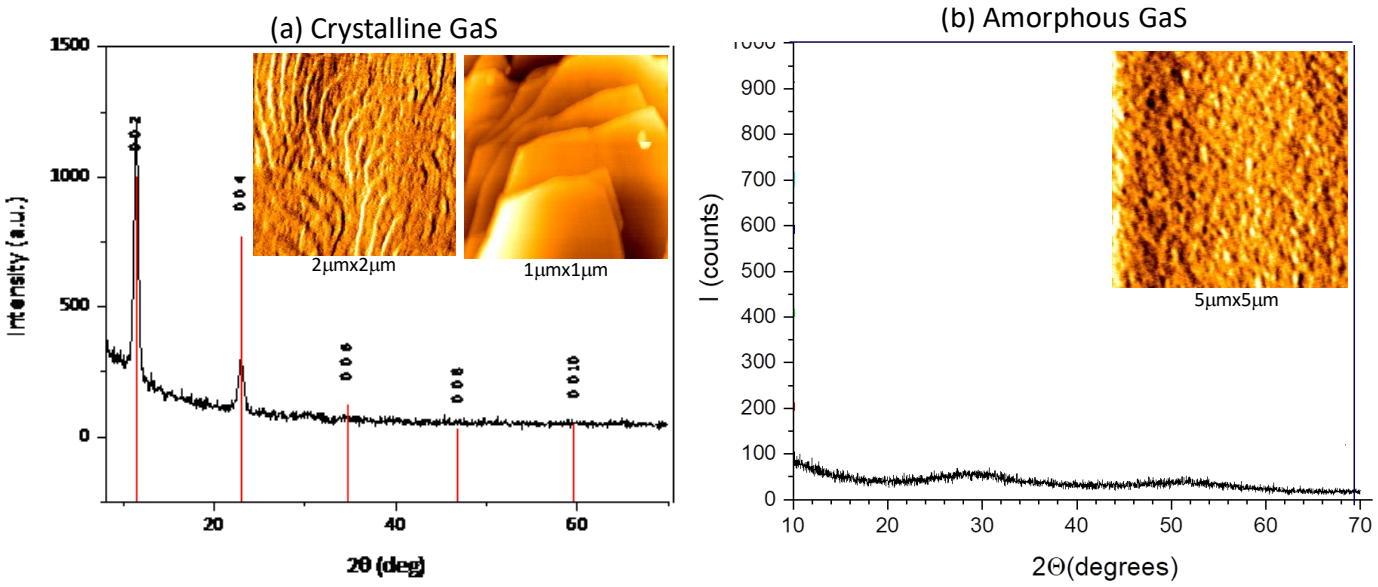

Figure 19: *XRD spectra for a typical (a) highly oriented CVD crystalline GaS sample deposited at 650°C and (b) CVD amorphous GaS sampledeposited at room temperature, both on sapphire substrate. The corresponding AFM morphologies are reported as inset.*

Figure 20 shows a series of SEM images about monolayer and few layers crystalline and amorphous GaS film further investigated by Raman and spectroscopic ellipsometry. This combined multi-characterization approach allows us to determine the interplay between structure and optical properties, needed to determine and/or predict the optical contrast during structural phase change.
GaS has three first-order phonon modes in the Raman spectrum. They are two out-of-plane A^1_{1g} and A^2_{1g} modes, and one in-plane E^1_{2g} mode. Interestingly, when going from crystalline to microcrystalline GaS the Raman spectra are dominated by the A^1_{1g} mode, until all modes are quenched for the amorphous films. Therefore, Raman spectroscopy is an appropriate diagnostic tool to monitor amorphous/crystallization phase transformation, while spectroscopic ellipsometry provides the corresponding change in the optical properties and, therefore, optical contrast, as summarized in Figure 20.
Therefore, different growth regimes from fully crystalline to amorphous of GaS have been identified and samples produced.

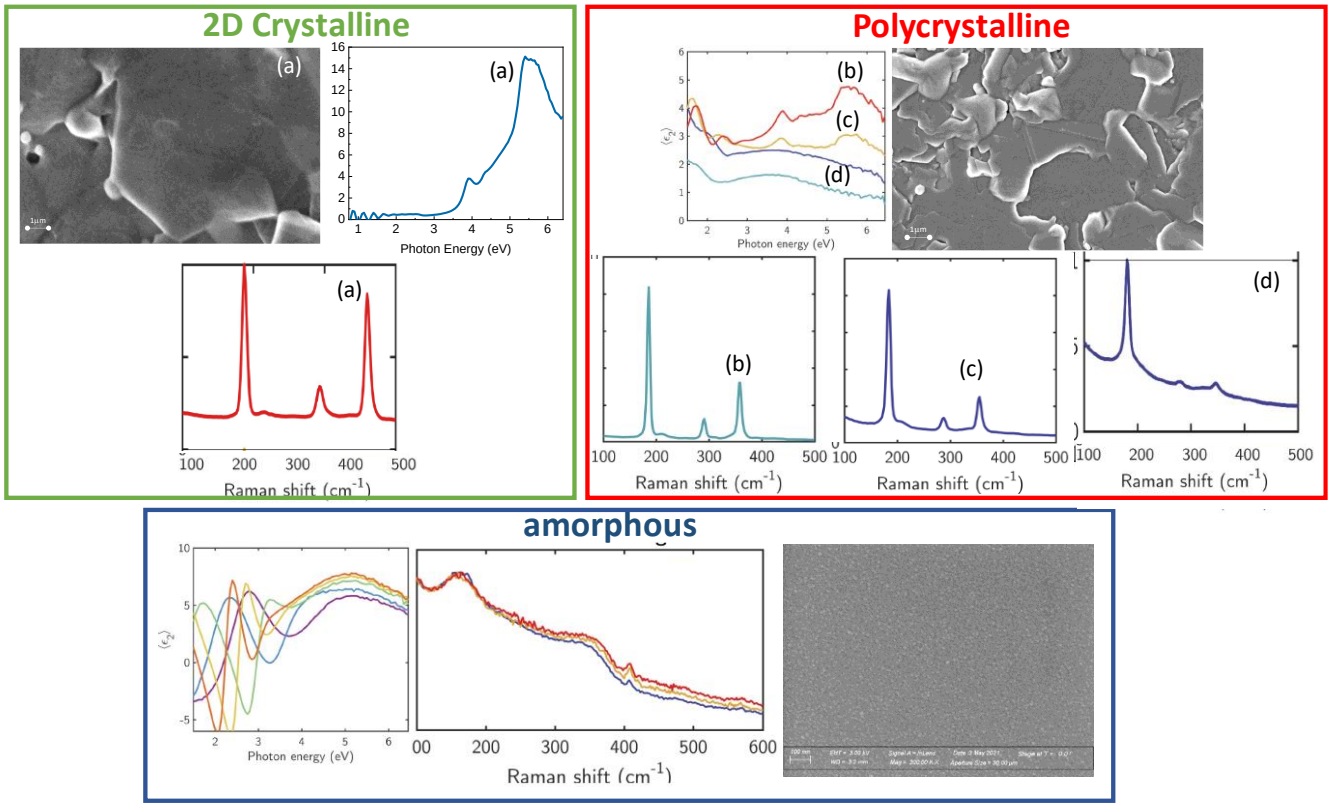

Figure 20: *Typical Raman and Ellipsometric spectra for the 2D crystalline GaS, polycrystalline GaS and amorphous GaS, whose typical SEM micrographies are also shown.*

Therefore, GaS has been identified within PHEMTRONICS has a novel optical phase change material to be further optimized within PHEMTRONICS.
The optical contrast that can be achieved by the amorphous-to-crystalline GaS and the order-to-order GaS-to-Ga_2S_3 transformation is shown in Figure 25.

The importance of identifying those growth regimes is evident considering that films with identified structure have been tested in phase transformation:

- We are able to operate the GaS amorphous –to-crystalline phase change by annealing and by green laser irradiation, as shown by theexamples in Figure 21 and Figure 22, together with the Raman and ellipsometry characterization upon phase change.
- Viceversa we are able to operate the GaS crystalline-to-amorphous phase change by green laser irradiation, as shown by 2 cycles of amorphous-crystalline transformation in Figure. 23.
- We are also able to operate the order-to-order crystalline GaS-to-Ga_2S_3 phase transformation by blue laser irradiation, as shown in Figure 24, yielding also appropriate optical contrast shown in Figure 25.

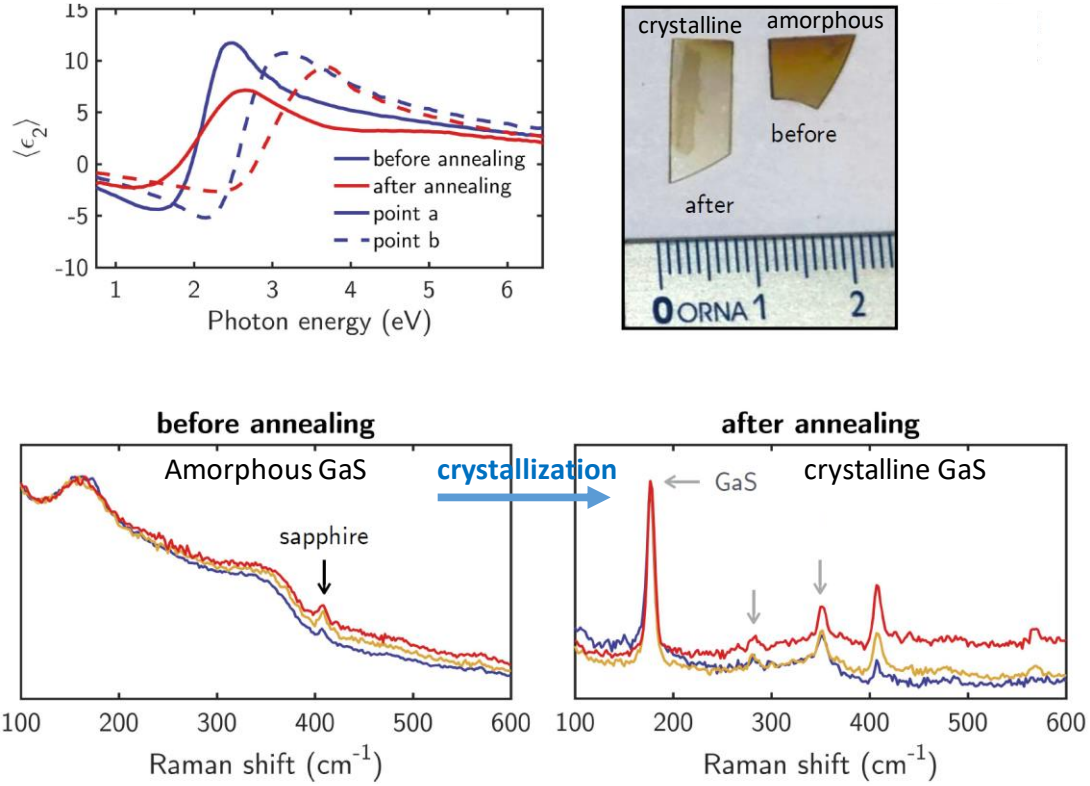

Figure 21: *Characterization structural-optical characterization of the amorphous-to-crystalline phase transformation by annealing*

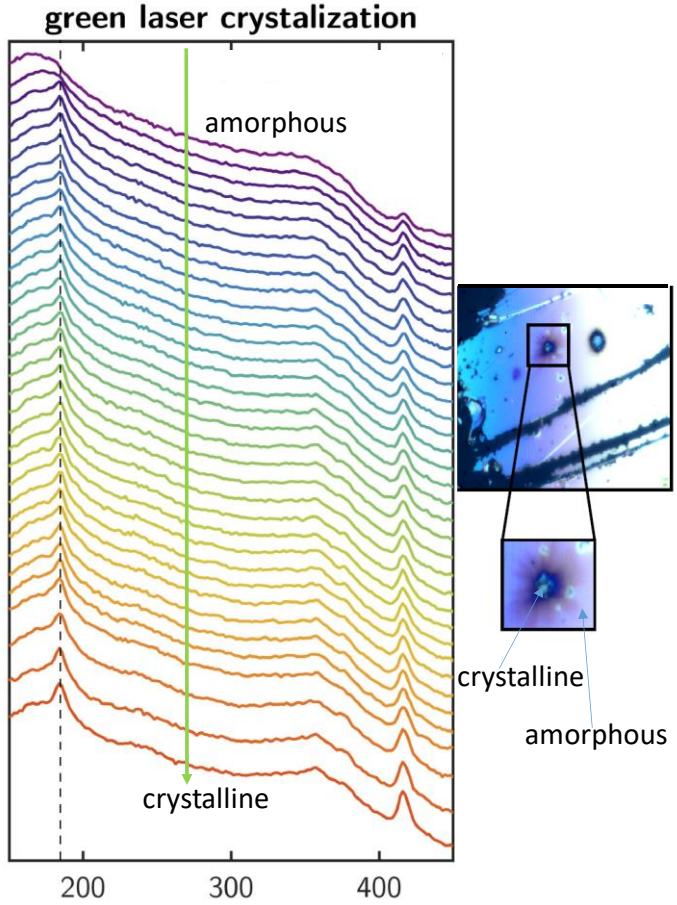

Figure 22: *Raman characterization structural-optical characterization of the amorphous-to-crystalline phase transformation by green laser pulses.*

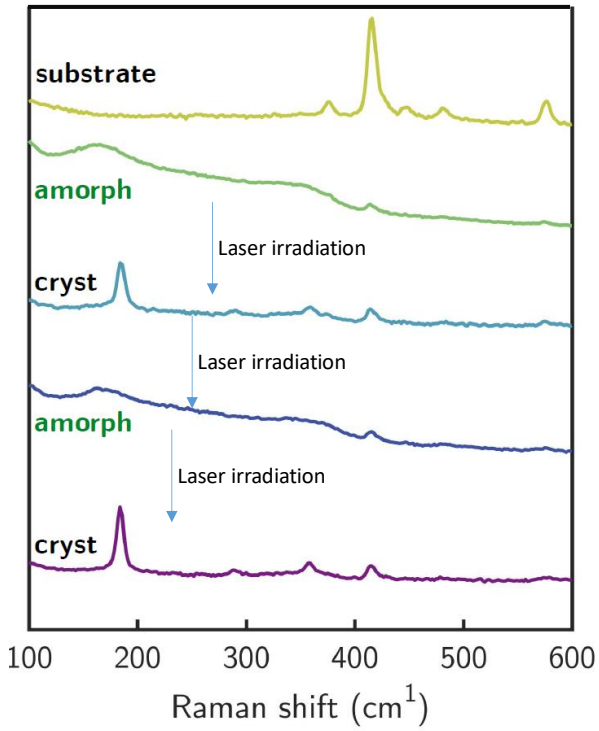

Figure 23: *Proof-of-concept of the amorphous-to-crystalline and viceversa phase transformation of GaS characterized by Raman spectroscopy.*

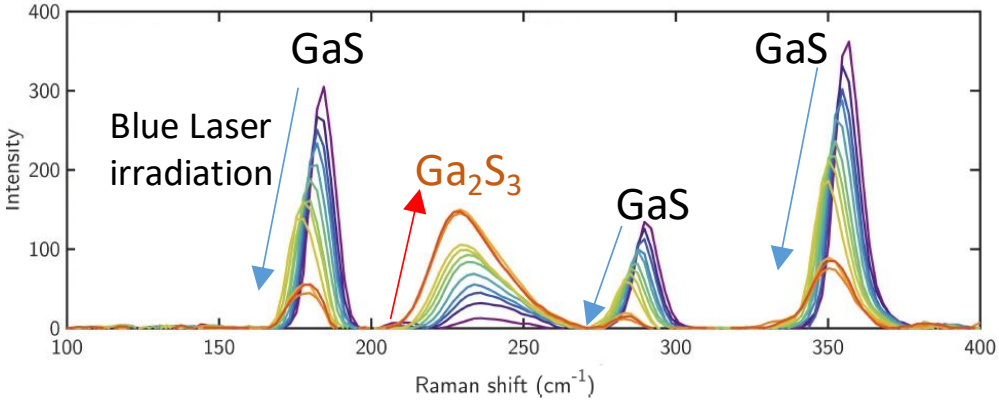

Figure 24: *Raman analysis of the order-to-order GaS to Ga_2S_3 phase transformation*

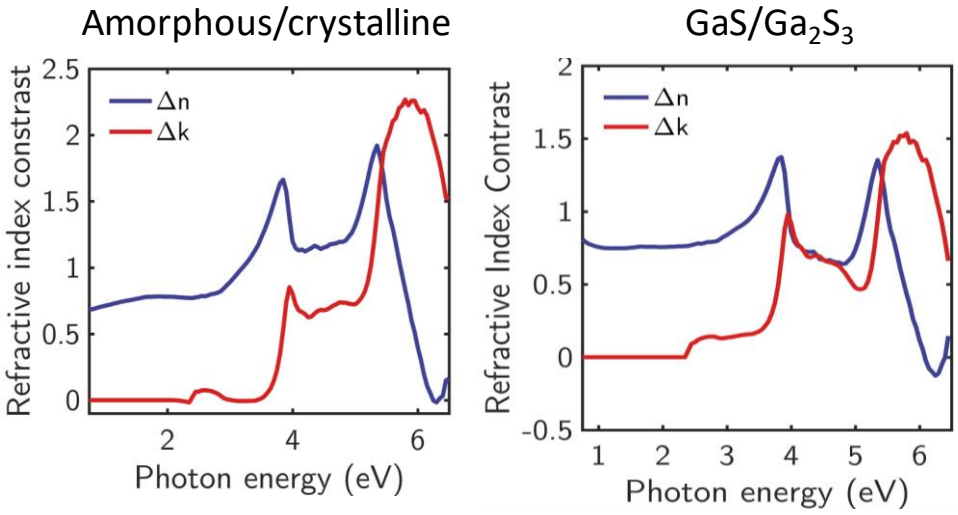

Figure 25: *Optical contrast achieved during the amorphous-crystalline and order-to-order phase transformation of GaS as characterized by spectroscopic ellipsometry*

6. Overview of Sb – Chalcohenides Sb_2S_3, SbS, Sb_2Se_3, Sb_2Te_3

Antimony chalcogenides are highly anisotropic V–VI group compounds that have wide applications in solar cells, photocatalysis, Li-ion batteries, thermoelectric conversion and other semiconducting areas. Sb_2S_3 and Sb_2Se_3 are two indirect band gap semiconductors that have emerged as very promising alternative absorber materials due to their suitable tunable bandgaps ranging from 1.1 to 1.8 eV according to the Se and S contents. They have crystal structures in the orthorhombic system (*Pbnm* space group) and are isostructural with Bi_2S_3. The crystal structure of Sb_2S_3 viewed along the [0 1 0] direction is shown in Figure 26. The Sb-S covalent bonds are indicated by solid lines, and the weak van der Waals bonds are marked by black-dashed lines. The cleavage trace is demarcated by a red-dashed line. The $(Sb_4S_6)_n$ building blocks form infinite 1D chains, separated by the lone pair electrons of the Sb and connected to each other by weak Sb-S interactions. Sb_2S_3 tends to form a 1D structure because specific S atoms are connected to the Sb of a second parallel chain by weak van der Waals bonds, which is responsible for the rupture of the crystal parallel to the *c*-axis direction in the [0 1 0] plane.
Typical properties of antimony chalcogenides are summarized in Table III.

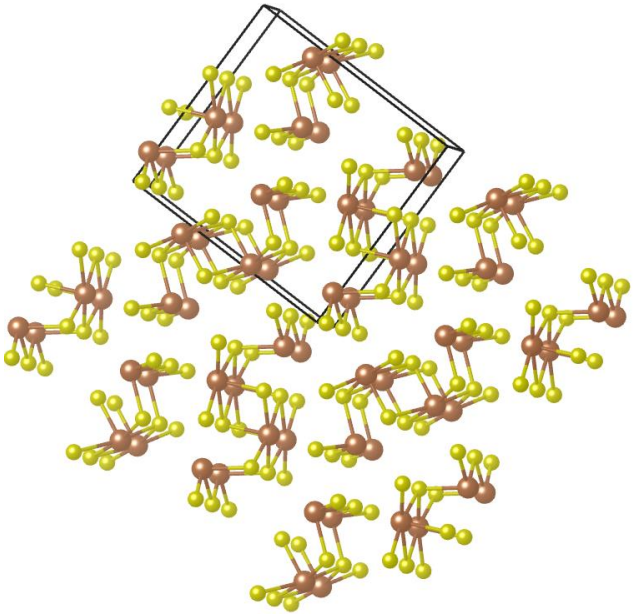

***Figure 26**: Layered structure of Sb-chalcogenides*

Property	Sb_2S_3	Sb_2Se_3
Crystal lattice (Å)	a: 11.57	a: 11.71
	b: 11.57	b: 11.62
	c: 3.83	c: 4.14
Space group	*Pnma 62*	*Pnma 62*
Density (g cm^{-3})	4.60	5.84
Melting point (K)	823	885
Absorption coefficient (cm^{-1})	10^4–10^5	>10^5
Band gap (eV)	Indirect gap 1.63	Indirect gap 1.03
	Direct gap 1.72	Direct gap 1.17
Dielectric constant	22	15.1
Conductivity ($(\Omega\ cm)^{-1}$)	5×10^{-6}	7×10^{-5}
Mobility ($cm^2\ V^{-1}\ s^{-1}$)	$\mu_e = 9.8$	$\mu_e = 15$
	$\mu_h = 10$	$\mu_h = 42$

***Table III:** Properties of Sb-Chalogenides*

6.1 Sb_2S_3 / SbS as phase change material candidate

In PHEMTRONONICS Sb_2S_3 has been selected as a potential phase change material candidate.
Sb_2S_3 was described as a write once, read many times (WORM)[24] material due to sulfur loss on phase change causing film degradation, and a bandgap higher than the diodes used for writing memory. However, an important recent work by Dong et al. has disputed this classification, showing phase stable switching with a bandgap of 2 eV.[25]
Chemical Bath Deposition (CBD) is a versatile, simple, inexpensive and convenient method for large area chalcogenide thin film synthesis.
Uniform, orange yellow, compact, semiconducting Sb_2S_3 films were obtained on glass and sapphire substrates using $SbCl_3$ solution as Sb^{3+} source and $Na_2S_2O_3$ solution as S^{2-} source. The main chemical reactions involved in this synthesis are the following:

[24] P. Arun, A. G. Vedeshwar, N. C. Mehra, *Mater. Res. Bull.* **1997**, *32*, 907.
[25] W. Dong, H. Liu, J. K. Behera, L. Lu, R. J. H. Ng, K. V. Sreekanth, X. Zhou, J. K. W. Yang, R. E. Simpson, *Adv. Funct. Mater.* **2019**, *29*, 1806181

$2SbCl_3 + 3Na_2S_2O_3 \text{ ---------> } Sb_2(S_2O_3) + 6NaCl$ (1)

$Sb_2(S_2O_3)_3 \text{ ---------> } 2Sb^{3+} + 3S_2O_3^{2-}$ (2)

$S_2O_3^{2-} + H_2O \text{ ---------> } SO_4^{2-} + S^{2-} + 2H^+$ (3)

$2Sb^{3+} + 3S^{2-} \text{ ---------> } Sb_2S_3$ (4)

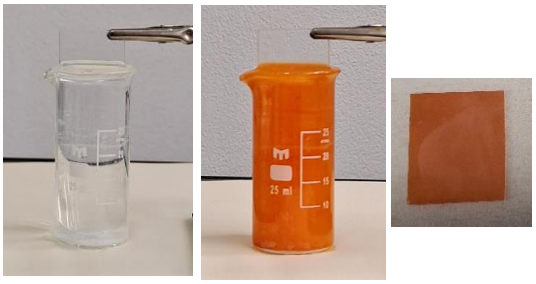

Figure 27 shows characteristic AFM image for a typical amorphous Sb_2S_3 film, as confirmed by preliminary diffraction measurements, SEM and TEM analyses. To get an image of the cross-section of the layers, a section of the sample was cut with a focused ion beam (FIB) of gallium ions. There are several layers visible:

- The thick and dark top layer was applied on top of the sample to protect the layers below so that a clean cut could be achieved.
- the upper layer of the two thin layers in the centre of the cut section is the Sb2S3 thin film with a layer thickness of around 330 nm. The film seems homogeneous with no visible crystallites confirming its amorphous nature. Surface roughness is clearly visible with a lateral size in the 100 nm range.
- The lowest layer is the bulk of the glass.

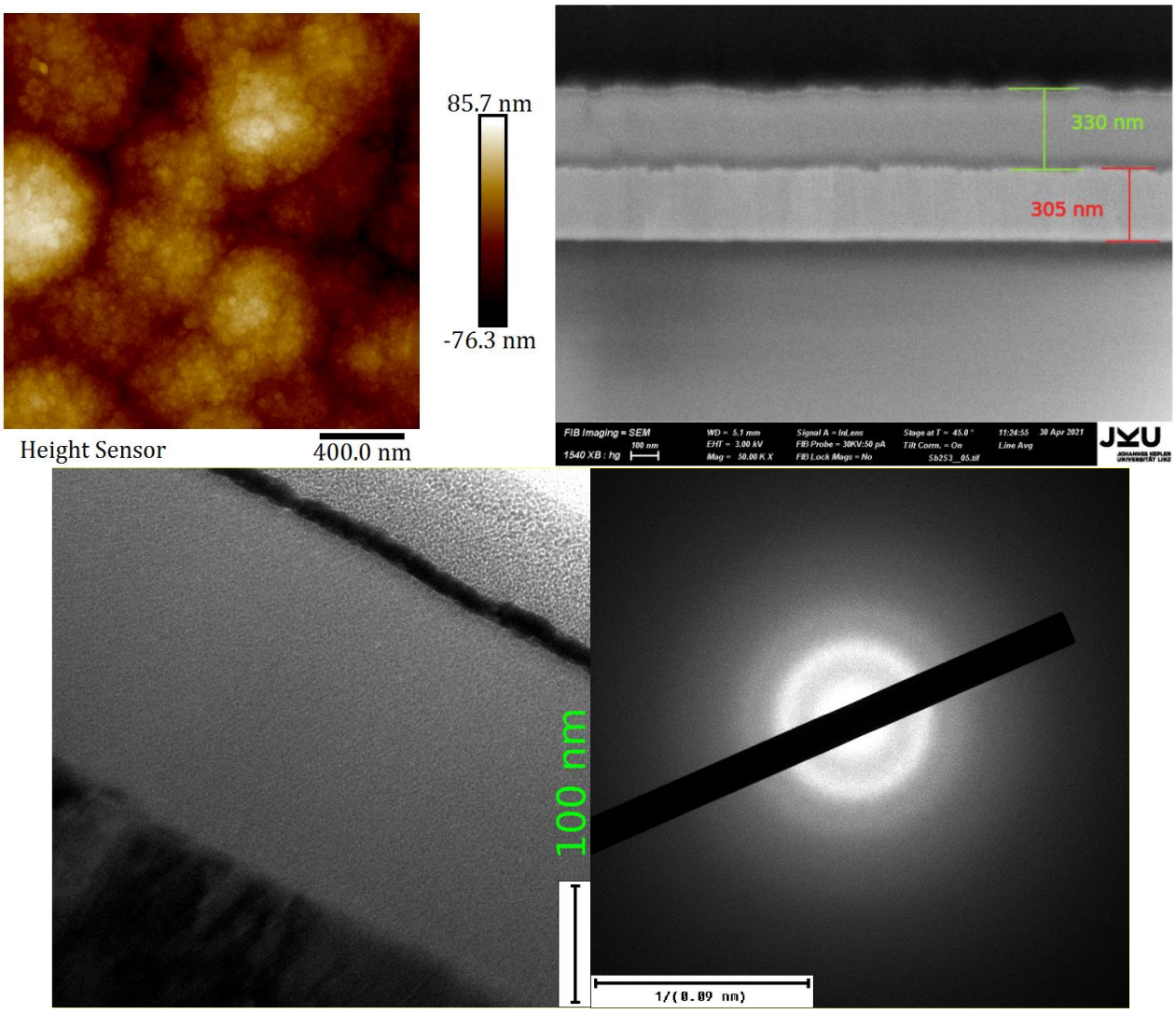

Figure 27: *(Top left) AFM image for Sb_2S_3 film on glass. RMS surface roughness (Rq) = 21.8 nm. Scan size= 2 x 2 μm (Top right) SEM cross section showing the homogeneous amorphous nature of the Sb_2S_3 film. Bottom left: zoom on Sb_2S_3 layer. Bottom right: electron diffraction pattern of Sb_2S_3 film shows washed out rings which is characteristic for amorphous materials.*

As for the optical properties, samples have been exchanged between partners to measure, reflectance, transmittance and ellipsometry. The characteristic optical transmittance spectra for Sb_2S_3 films grown on glass are presented in Figure 28. The (αhυ) 2 is plotted against the photon energy (hυ) to infer information about the onset of absorption. It has been observed that the band gap decreases with increase in Sb concentrations.

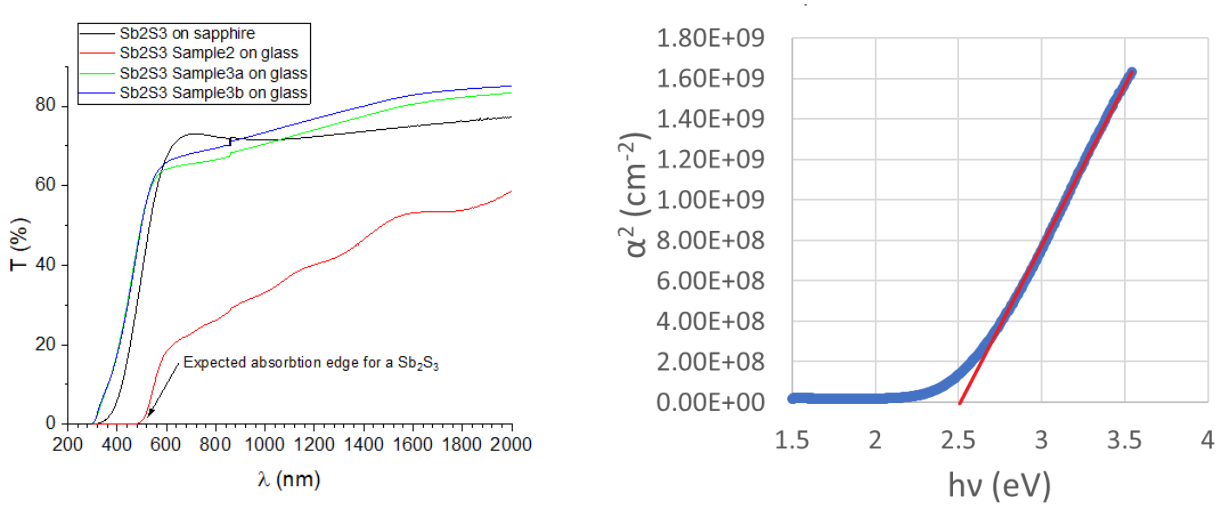

Figure 28: *UV-VIS-NIR optical transmittance measured in normal incidence for Sb_2S_3 film on a glass substrate.*

Further investigation of optical properties has been carried out by ellipsometry. The determination of the dielectric function and the layer thickness with ellipsometry alone in an unambiguous way was very challenging, since the Sb_2S_3 film could be optically anisotropic, like single-crystalline Sb_2S_3.
The previous AFM/STEM and microscopy investigations in Figure 27 have been used to guide the construction of a physically reasonable and appropriate optical model and determine the optical constants under the assumption that the Sb_2S_3 film is amorphous, homogeneous and isotropic. The dielectric function, refractive index, n, and extinction coefficient, k, of amorphous Sb_2S_3 are shown in Figure 29.
Important aspects of the dielectric function are:

- optical absorption starts above 2 eV (see k in green above)
- the refractive index below the absorption range is between 2.3 and 2.7, which is rather low for a material with ”high” refractive index. The refractive index of single crystalline Sb_2S_3 is much higher.
- at the start of the absorption slightly above 2 eV, there is and interesting structure and around 1 eV

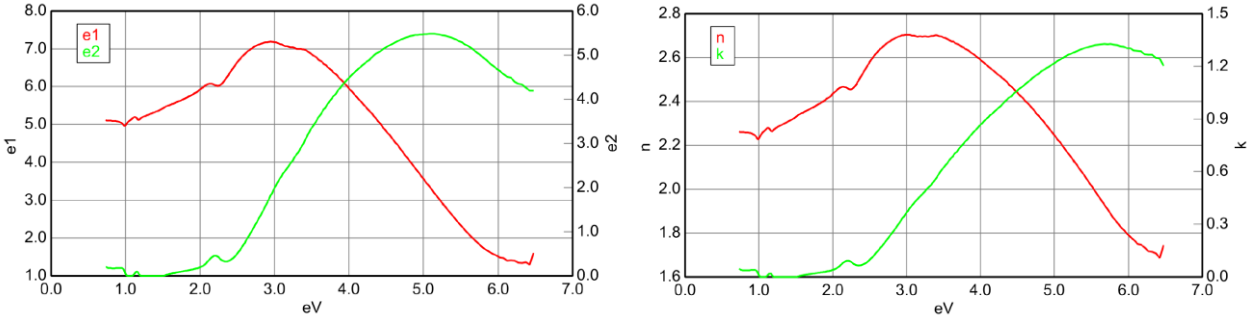

Figure 29: *(left) Dielectric function, (right) refractive index and extinction coefficient of amorphous Sb_2S_3*

For the Raman measurement on Sb_2S_3 film on glass two different Raman systems have been used, the first one (Invia Reflex Renishaw) uses a green laser excitation (514nm), and the second, an FT Raman (Thermo Fisher Scientific) use a NIR laser (1064nm). The measurements have been repeated on at least ten different sites and the characteristic Raman spectra for Sb_2S_3measured with 514nm and 1064nm laser excitation are shown in Figure 30. It was found that Sb_2S_3 film is highly sensitive to the 514nm laser line and therefore measurements have been performed at very low laser power. The use of 1064nm laser excitation allows avoid heating effects in Sb_2S_3 film as this laser line is below the Sb_2S_3 bandgap. For lower green laser excitation (≤0.2mW) the Raman spectrum shows two broad phonon modes that are characteristic for a disordered Sb_2S_3

film (polycrystalline-like structure). This is confirmed by FT Raman measurements made with 1064nm laser excitation (see the green trace in Figure 30) the confirm the presence of stibnite (Sb_2S_3). When green laser power is increased above 2mW a phase transition occurs and we can see the presence of Sb and of α- Sb_2O_3.

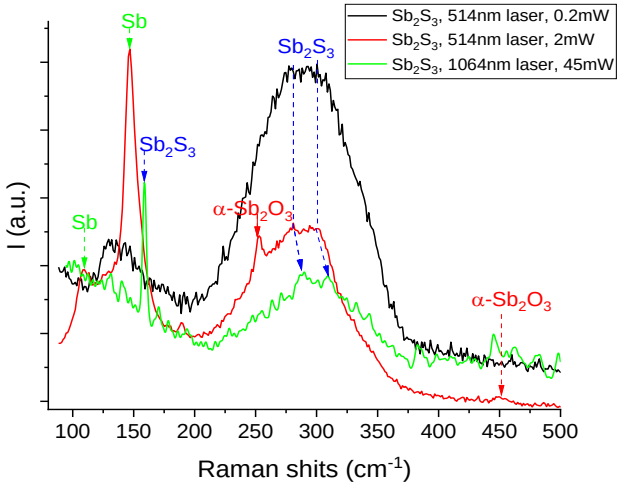

Figure 30 *Raman spectra for Sb_2S_3 film on glass substrate obtained using two different laser excitations: a)514nm (0.2mW and 2mW) 1064nm (45mW)*

The Raman mapping of Sb_2S_3 film on glass shown in Figure 31 shown that this phase transition is highly reproducible for green laser power above 2mW.

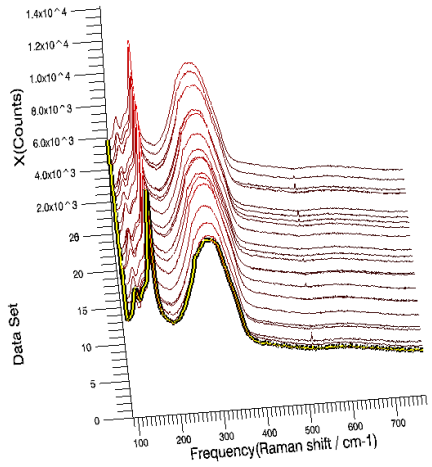

Figure 31 a) *3D Raman mapping Sb_2S_3 film on glass using green laser excitation (514nm, 4mW)*

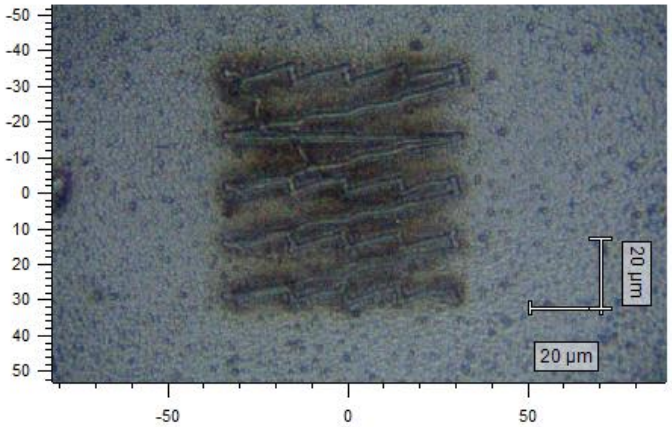

Figure 31: b) *Optical image of Sb_2S_3 film on glass after laser scribing using green laser excitation (514nm, 4mW)*

The preliminary results on the phase transition in Sb_2S_3 show that further study is required about laser to identify the laser wavelength and irradiation conditions to be used to avoid strong photothermal effects

We have done preliminary experiments of laser induced phase change using low power optical pulses from a diode laser to reversibly crystallize and amorphize the Sb_2S_3. By using the proper wavelength and power that avoids thermal effects, the amorphous-to-crystalline phase transition can be achieved as shown in Figure 32. The reversible switching requires a critical amount of absorption in the materials to achieve the required temperature states. In particular, Sb_2S_3 shows very low absorption at visible wavelengths (λ =633 nm), which introduces challenges for optical switching. An example of the optical properties change upon laser crystallization and phase transformation is also shown in Figure 32 by the ellipsometric spectra of the film pseudodielectric function, giving a proof-of-concept that Sb_2S_3 could be explored as an optical phase change material.

The substitution of sulfur with selenium in Sb_2Se_3 shifts the absorption edge into the visible range without compromising the low absorption at telecommunication wavelengths. The conditions for all-optical switching in both phases are being tested using optical pulses with tunable pulse length and power, and both thermal crystallization and fast amorphization are demonstrated.

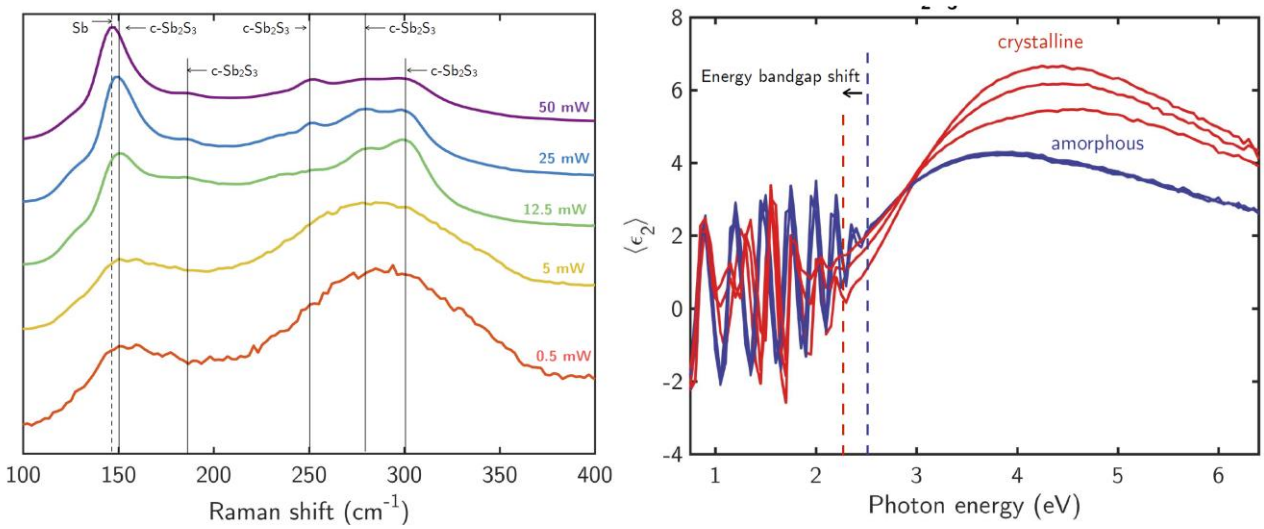

Figure 32: *(left) Raman characterization of the characterization of Sb_2S_3; (right) Ellipsometric spectra of the imaginary part of the pseudodielectric function before and after Sb_2S_3 crystallization.*

Extracting and comparing the optical constants of amorphous and crystalline Sb_2S_3 the wavelength dependent contrast of refractive index and extinction coefficient has been determined as shown in Fig. 33.

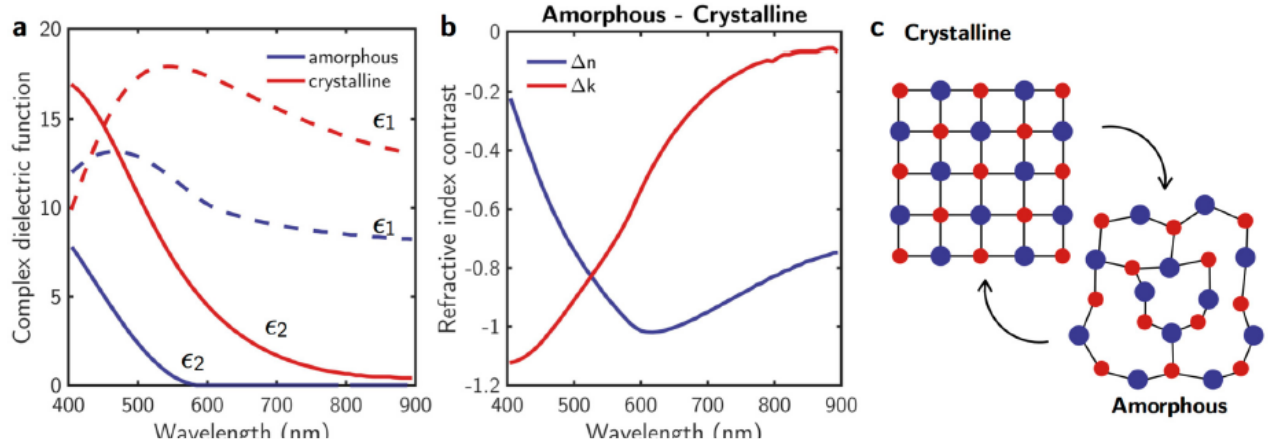

Figure 33: *(a) Complex dielectric function of amorphous and crystalline Sb_2S_3 upon laser cycles of crystallization/crystallization as obtained by ellipsometry measurements; (b) derived figure of merit of optical contrast between the amorphous and crystalline phases.*

In addition to laser induced phase change, Sb_2S_3 can also phase change by thermal annealing, as shown in Figure 34

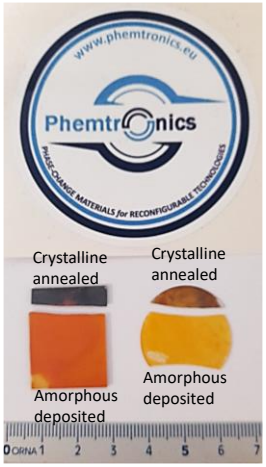

Figure 34: *Pictures of Sb_2S_3 amorphous-crystalline phase change upon annealing*

An original approach and contribution that PHEMTRONICS is developing is based on the imaging polarimetry in transmission. As shown in Figure 35 for the Sb_2S_3 as deposited (amorphous) and after annealing (crystallization), the extent of crystallization can be mapped and visualized, the crystallites identified and their contribution to birefringence and dichroism quantified. Furthermore, the measured difference in transmission between the amorphous part and the crystallites allow to determine the contrast in optical properties upon the phase transformation, without any assumption on the dielectric function of the sample. A good contrast in transmittance between crystalline and amorphous phases at 550 nm which is the goal of PHEMTRONICS is achieved.

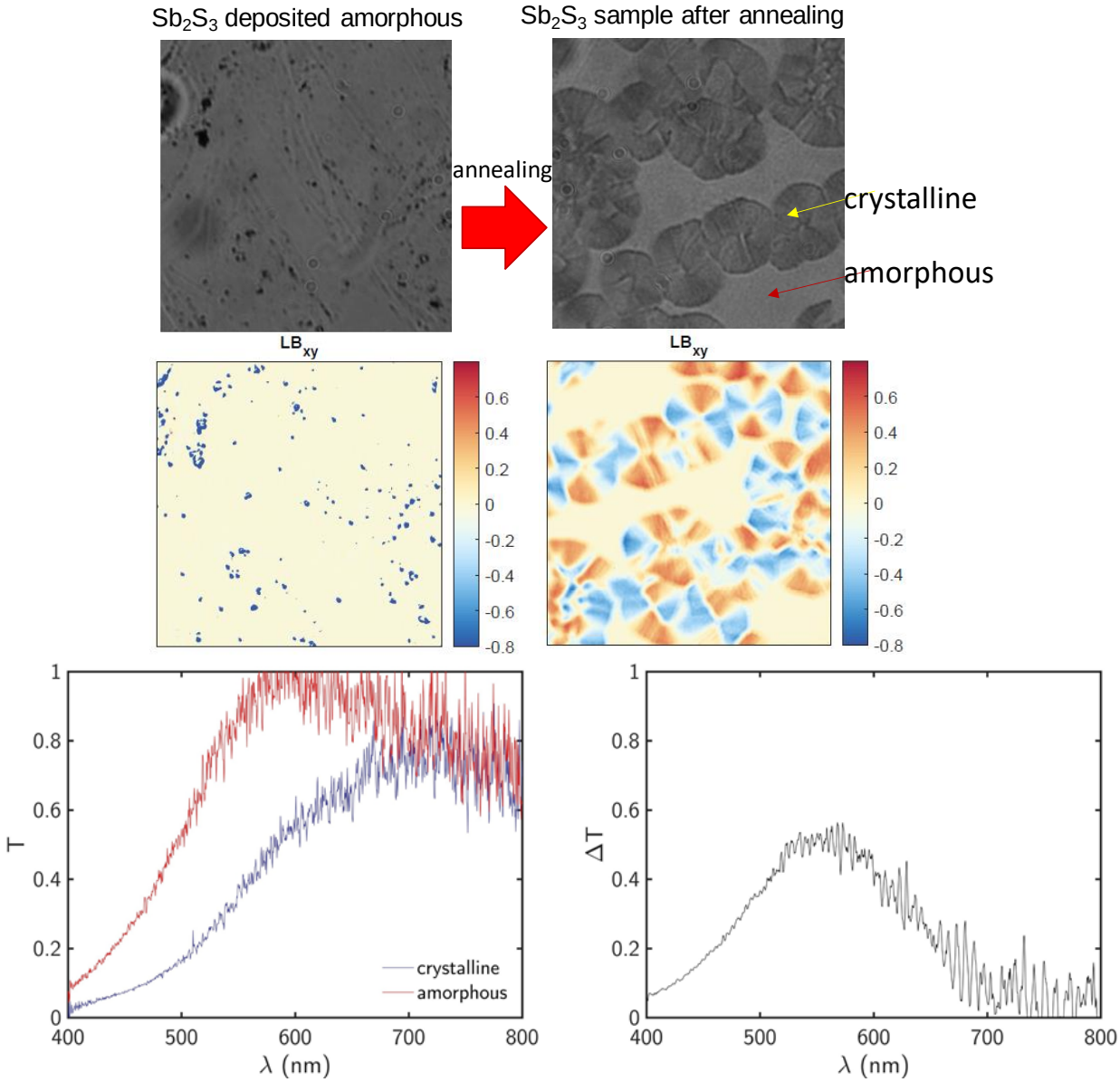

Figure 35: *(a) Optical micrographs and linear xy birefringence maps for amorphous and crystallized Sb_2S_3 film. The transmittance of the amorphous and crystalline phases with the resulting optical contrast between the two phases shown on the right*

Therefore, since the demonstration that both Sb_2S_3 and Sb_2Se_3 films can be switched repeatedly using a visible laser, between the amorphous and crystalline phases Sb_2S_3 has been selected for further consideration as phase change material.
Phase switching of Sb_2S_3 and Sb_2Se_3 was found to be highly dependent on film quality and local topology. Therefore, the activity will continue on optimizing Sb_2S_3 and Sb_2Se_3 by both chemical bath and CVD to better understand and control the interplay between the film quality and cyclability of phase change.

7. 2D group IV–IV monochalcogenides

At room temperature, the monolayer structures of 2D group IV–IV monochalcogenides GeS, GeSe, SnS and SnSe exhibit a thermodynamically preferred phase of an orthorhombic α structure. Structural transformations between the different phases induce the large changes in the electroninc properties and applications of 2D group IV–IV monochalcogenide (GeS, GeSe, SnS and SnSe) semiconductors.
2D group IV–VI monochalcogenides (GeS, GeSe, SnS and SnSe) with the same crystal structure of SnTe revealed that the unique ionic-potential anharmonicity can induce spontaneous in-plane electrical polarization and ferroelectricity.[26] Based on this, Xiong et al proved that the phase structures play an important role in the stability and polarizations. 2D group IV–IV monochalcogenides have four degenerate structural ground states, and a phase transition from a threefold coordinated with a fivefold coordinated structure takes place at finite temperature. Understanding the phase transition correlation between structure distortions, spontaneous polarization and the chemical bonding nature is important for predicting new ferroelectric materials and for nonlinear optical properties of materials such as second- and higher-order harmonic generation, which play pivotal roles in lasers, frequency conversion, electrooptic modulators and switches. Recently, Wang et al[27] predicted giant SHG in recently discovered 2D ferroelectric-ferroelastic multiferroic group IV monochalcogenides (i.e. GeSe, GeS, SnSe and SnS). Remarkably, the strength of SHG susceptibility in GeSe and SnSe monolayers has been proved to have more than one order of magnitude higher than that in monolayer MoS2. These present findings provide a microscopic understanding of the large SHG susceptibility in 2D group IV monochalcogenide multiferroics and can open a variety of new avenues for 2D ferroelectrics, multiferroics and nonlinear optoelectronics, for example, realizing active electrical/mechanical switching of ferroic orders in 2D multiferroics and in situ ultrafast optical characterization of local electronic structures using non-contact non-invasive optical SHG techniques
Despite some theoretical and experimental studies of α-form group IV–IV monochalcogenide GeS, GeSe, SnS and SnSe monolayers being reported, many important questions remain unanswered.

7.1 GeS as phase change material candidate.

GeS (Germanium sulfide) is a 2D narrow-indirect bandgap (1.65 eV) semiconductor or semimetal, which has potential implications for various optoelectronic applications.
GeS is a polymorph material. At room temperature, the thermodynamic preferred phase of GeS is that of the orthorhombic α-GeS structure (a = 10.47 Å, b = 3.64 Å, c = 4.30 Å). The α structure undergoes a phase transition at 600 K and transforms into a hexagonal β-GeS structure (a = b = 8.70 Å, c = 8.73 Å), as shown in Figure 34. Above 873 K, the α structure undergoes a phase transition to the β-GeS structure (a = 4.24 Å, b = 10.45 Å, c = 3.69 Å).[28]
Figure 36 shows the structure of the orthorhombic and monoclinic phases of GeS.
Only recently it was reported that GeS undergoes an **insulator-semiconductor–metal phase transition** (seven orders of magnitude in resistivity difference between an insulator and metallic phases) at room temperature and high pressure[29].
The potential of optically or photothermal induced insulator-semiconductor–metal phase transition in GeS will be investigated in PHEMTRONICS with a view of using it in optoelectronic plasmonic-based devices and as well for the realization of microwave devices such as switches or phase shifters. As such, the presence or absence of optically or photothermal induce phase transitions in GeS compounds is still uncertain, resulting in an incomplete understanding of the transition pathway.

[26] Xiong F, Zhang X, Lin Z and Chen Y Ferroelectric engineering of two-dimensional group-IV monochalcogenides: the effects of alloying and strain J. Materiomics 4 139–43 (2018)
[27] Wang H and Qian X Giant optical second harmonic generation in two-dimensional multiferroics Nano Lett. 17, 5027–34 (2017)
[28] P. D. Antunez, J. J. Buckley and R. L. Brutchey Tin and germanium monochalcogenide IV–VI semiconductor nanocrystals for use in solar cells Nanoscale 3 2399–411 (2011).
[29] Choong-Shik Yoo et al, Structural transitions and metallization in dense GeS, PHYSICAL REVIEW B 93, 104107 (2016)

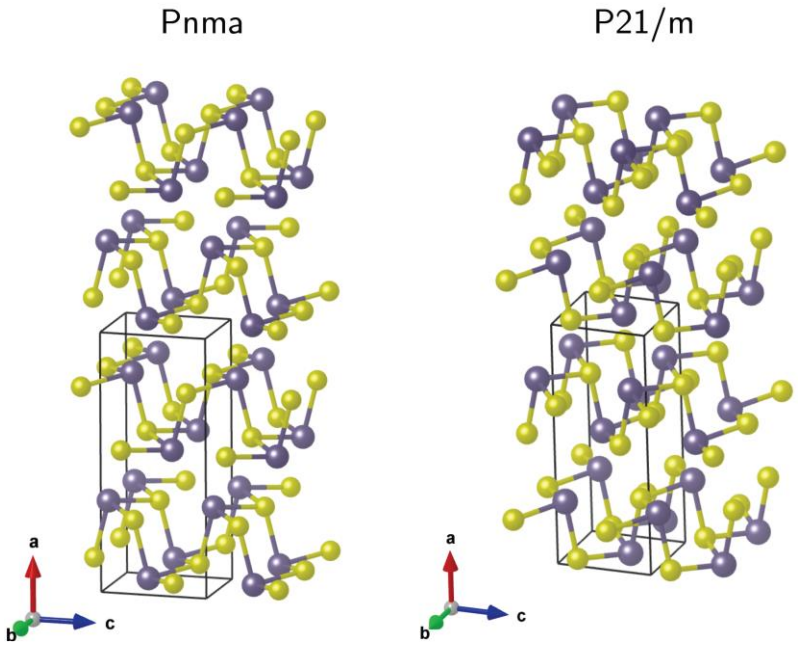

Figure 36. *Crystal models of various phases of GeS[1]. (left) (a) Orthorhombic structure in Pnma of phase I, (b) monoclinic, and (right) structure in P21/m of phase II. The dotted line represents the nearest neighboring intermolecular Ge-S distance.*

A factor-group analysis of the 3D space group D_{2h}^{16} reveals 24 vibrational modes for GeS [30]. Their representation at the center of the Brillouin zone is Γ= $4A_g + 2B_{1g} + 4B_{2g} + 2B_{3g} + 2A_u + 4B_{1u} + 2B_{2u} + 4B_{3u}$. Apart from three acoustic vibrations, there are 21 optical phonons: two are inactive ($2A_u$), seven are infrared active ($3B_{1u}$,$3B_{3u}$,$1B_{2u}$), and 12 are Raman active ($4A_g + 2B_{1g} + 4B_{2g} + 2B_{3g}$). The structure consisting of double layers (perpendicular to the c axis) are covalently bonded and forms a zigzag chain along the direction of the minor axis of the crystal in which Ge and S atoms are threefold coordinated to each other. According to the previous reports, at ambient conditions, Raman frequencies could be grouped into three lowest frequencies, (~52, ~64, and ~77 cm^{-1}), intermediated frequencies (ranging from ~88 cm−1 to ~133 cm^{-1}), and higher frequencies (ranging from ~210 cm^{-1} to ~300 cm^{-1}).
Within PHEMTRONICS we have started characterizing highly crystalline few layers GeS usingas starting material GeS single crystal (from HQ Graphene) shown in Figure 37. In this way, PHEMTRONICS will contribute towards building an intra-consortium material database on the optical and vibrational properties of GeS.

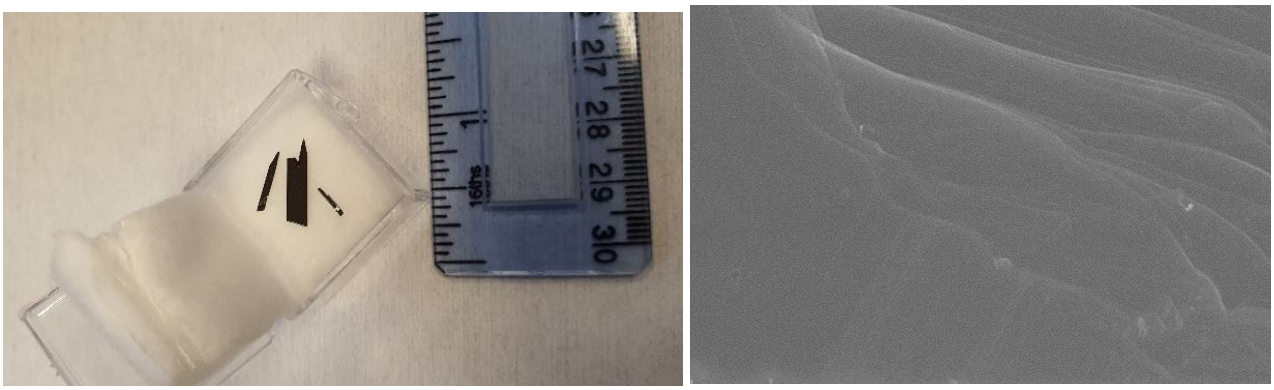

Figure 37. *Optical image of single-crystal GeS (around 1cm x 0.5cm) and SEM picture showing its layered structure*

[30] a) J. D. Wiley, W. J. Buckel, and R. L. Schmidt, Phys. Rev. B 13, 2489 (1976); b) G. Burns and A. M. Glazer, Space Groups for Solid State Scientists (Academic Press, New York, 1978).

for the Raman measurement on GeS single-crystal two different Raman systems have been used, the first one (Invia Reflex Renishaw) use a green laser excitation (514nm), and the second, an FT Raman (Thermo Fisher Scientific) use a NIR laser (1064nm).
The measurements have been repeated on at least ten different sites and the characteristic Raman spectra for GeS measured with 514nm and 1064nm laser excitation are shown in Figure 38. It was found that GeS is highly sensitive to the 514nm laser line and therefore measurements have been performed at very low laser power. The use of 1064nm laser excitation allows avoiding heating effects in GeS as this laser line is below the GeS bandgap.
The lowest frequency modes occur at 111 cm^{-1} (A_g shear mode) and have been seen only with 1064nm laser excitation. All other Raman phonon modes (with one exception of that located at 129cm^{-1}) correspond with that of orthorhombic structure in P_{nma} of phase I for GeS.

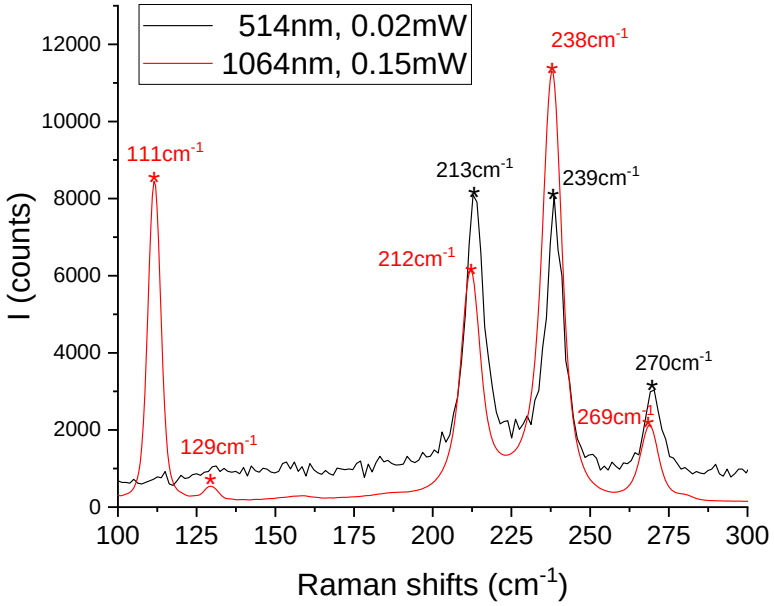

Figure 38. *Characteristic Raman spectra for GeS monocrystal measured with 514nm and 1064nm laser excitation*

The reproducibility of the Raman spectra on GeS is put in evidence in Figure 39 where 3D and 2D Raman mapping measurements (λ_{laser}=514nm, 0.02mW, 8s integration time) are presented.

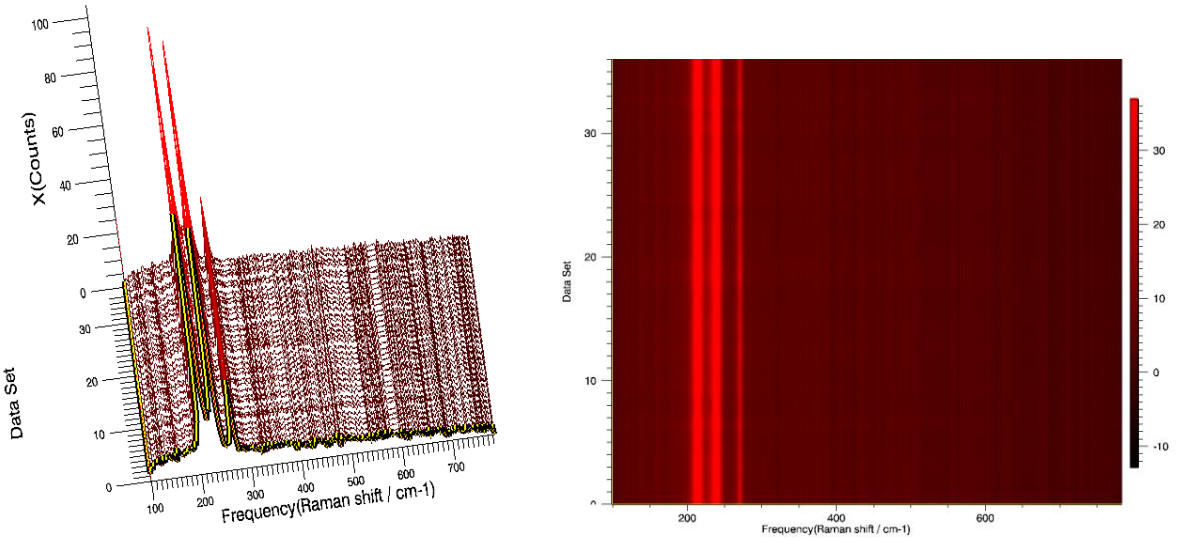

Figure 39*. 3D and 2D Raman mapping measurements (λ_{laser}=514nm, 0.02mW, 8s integration time)*

GeS monocrystal was found to be sensitive to the green laser power used in the Raman measurement undergoing a fast phase transition when green laser power reaches 2-4mW as shown in Figure 40. The identification of the exact new phase of GeS will require further investigation but we expect that we have a ***crystalline-to-crystalline*** **phase transition** from the orthorhombic structure in *Pnma* of phase I (an insulating GeS phase) to the monoclinic structure in P21/m of phase II (a semiconducting GeS phase). The crystal models of orthorhombic and monoclinic structure phases of GeS are shown in Figure 36.
Therefore, GeS has been identified as a potential phase-change materials activated by laser irradiation. Further investigation of this material is in progress.

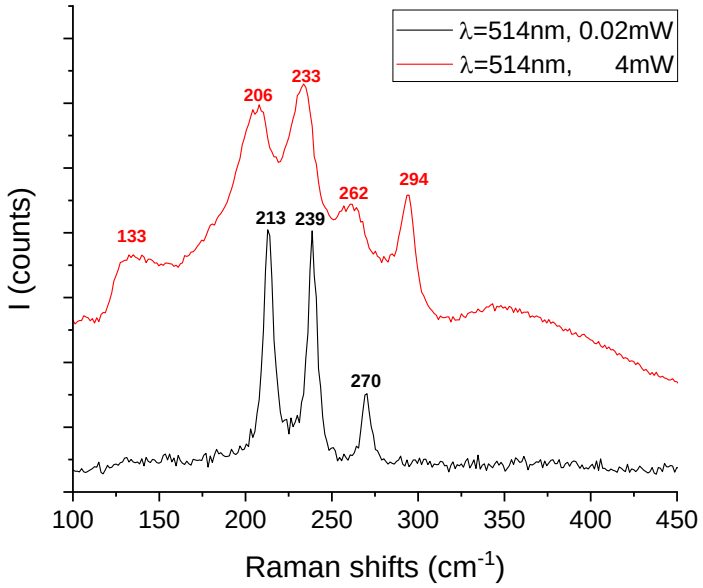

Figure 40. *Characteristic Raman spectra for GeS monocrystal using a green laser (514nm) and laser power of 0.02 and 4mW. Upon using green laser power of 4mW orthorhombic GeS undergoes a crystalline-to-crystalline phase transition*

The GeS orthorhombic monocrystal optical constants have been obtaining from spectroscopic ellipsometry measurement and are presented in Figure 41. As shown in Figure 42 we have obtained an optical bandgap of 1.55±0.05 eV for GeS orthorhombic monocrystal in good agreement to previously reported one (1.6 eV).

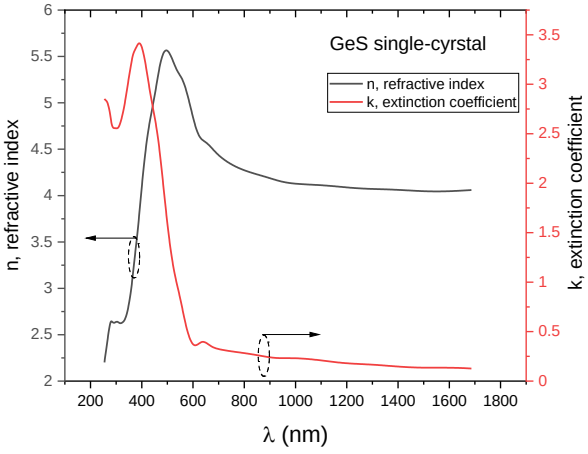

Figure 41 *Optical constants for GeS orthorhombic monocrystal*

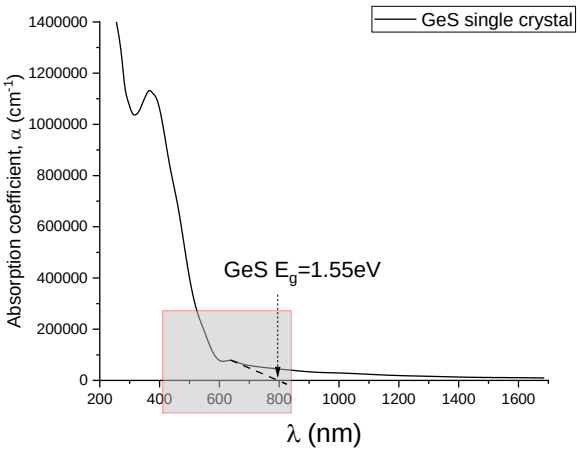

Figure 42. *The dispersion of the absorption coefficient, α, for GeS orthorhombic monocrystal*

Furthermore, we have investigated the direct sulphurisation of Ge as an alternative route for obtaining GeS. The first round of experiments has not been successful as shown in Figures 43a and 43.b where representative AFM and SEM images are shown. These indicated that Ge sulphurisation process was lead to an incomplete surface coverage with a GeS_{1-x} layer.

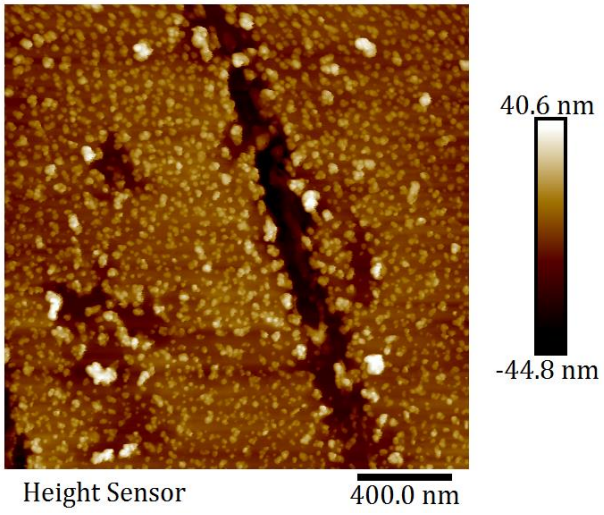

***Figure 43.a**: AFM image of the GeS_{1-x} sample. AFM RMS surface roughness (Rq) = 10.2 nm*

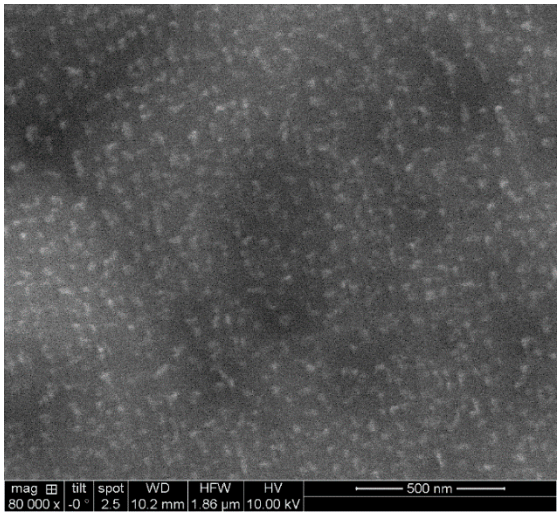

***Figure 43b:** SEM image of the GeS_{1-x} sample*

Nevertheless, further experiments will be run to achieve few layers of GeS directly integrated on germanium wafers, used in several electronic and optoelectronic platforms.

TNI-UCC plan to start developing an ALD process for GeS was delayed due to the Covid-19 pandemic situation. TNI-UCC has planned to upgrade a 200mm Picosun ALD reactor with H_2S gas line and a new distribution line for the Ge ALD precursors. The work is currently delayed due to the Covid-19 pandemic situation as external contractors are not allowed to come on-site to perform the upgrade work required. This is now rescheduled to be completed in Year 2 of the PHEMTRONICS project.

8. Overview of TMD Molybdenum Chalcogenides: MoS_2 and MoOx

TMDs exhibit various crystal structures with unique properties. In this regard, TMDs with phase-related properties make them more valuable to basic studies of many physical phenomena. Generally, based on the arrangement of atoms, monolayer TMDs show diverse structures, including H-phase and T- (or T'-) phases with different symmetry[31] as shown in Figure 44. H-phases with semiconducting characteristic are the most common ground state structure in the TMDs. The T-phase of materials such as MoS_2 is metastable, and it can be spontaneously converted into the H-phase under the stimulation of external conditions. Hence, the controlled preparation of metallic phase is still a great challenge, especially to obtain samples with higher quality and better stability.

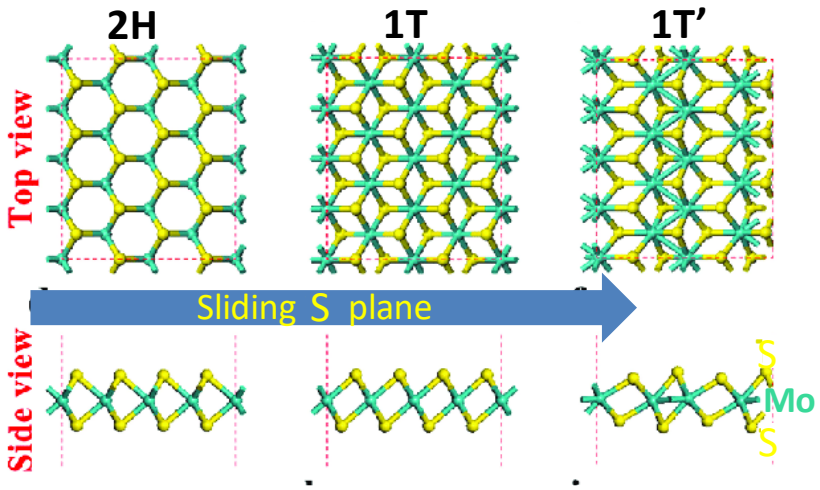

Figure 44: *semiconducting 2H to metallic 1T' phase transformation in 2D TMDs.*

8.1 2D MoS_2 as phase change material candidate.

MoS_2 is an emerging potential candidate as phase change material. Following 2D MoS_2 phase transition from trigonal prismatic 2H to octahedral 1T to 2H phases a large refractive index difference (Δn) is predicted[32] as shown in Figure 45.

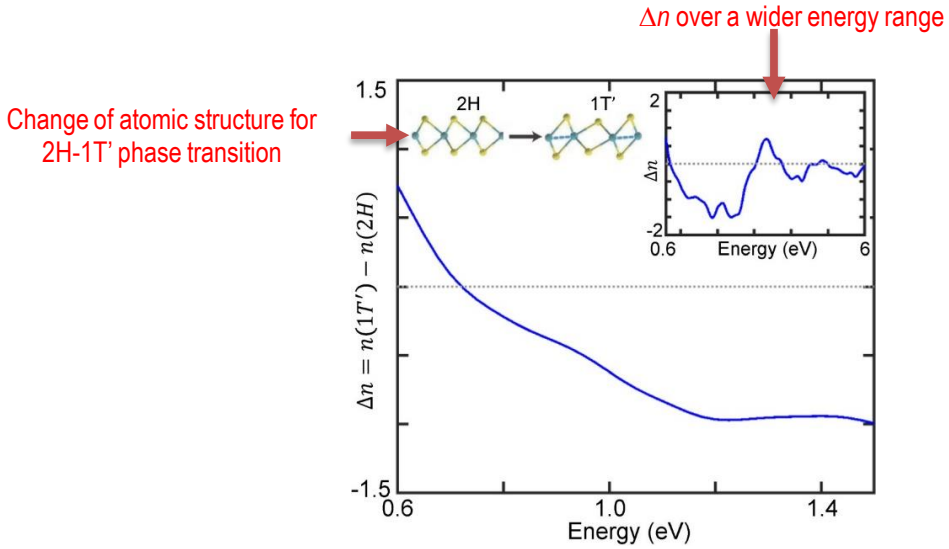

Figure 45: *Refractive index difference (Δn) between the 1T' and 2H phases of bulk MoS_2 in NIR*[4]

[31] Huang, H. H., Fan, X., Singh, D. J., & Zheng, W. T. (2019). *Recent Progress of TMD Nanomaterials: Phase Transitions and Applications. Nanoscale.* doi:10.1039/c9nr08313h

[32] Akshay Singh, et al, Appl. Phys. Lett. 115, 161902 (2019); doi: 10.1063/1.5124224

The MoS_2 Δn predicted to be comparable to or larger than that realized by phase-change materials in the GST system, $\Delta n \approx 1$ throughout the NIR (photonics application relevant). One particular, the aspect that will be further investigated in PHEMTRONICS in Year 2 will be the control of phase transition between 1T' and 2H phases of few-layers MoS_2. Recently TNI-UCC have reported that this can be achieved due to the fact that 2D MoS_2 behaves as a strain-induced ferroelectric material[33] (see Figure 46). MoS_2 self-switching diodes behave as lateral memristors and as photodetectors in the visible spectrum, with responsivities as high as 17 A/W[5].

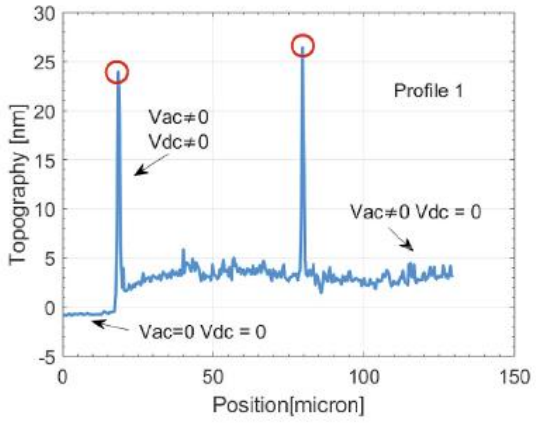

Figure 46a: *Topography of 7ML MoS_2 obtained during AFM[5]. An induced reversible phase transition from 2H to 1T phases takes place on an applied voltage.*

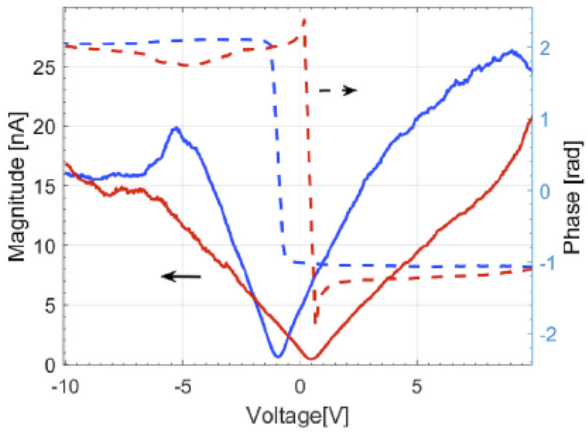

Figure 46b: *Piezo-force amplitude and phase curves obtained for a 0.5V AC voltage applied to the tip during PFM measurements[5].*

Within PHEMTRONICS, we have developed a well-controlled CVD growth process at 4-inch wafer-scale Si (sapphire) for 2D MoS_2, using $Mo(CO)_6$ and H_2S as precursors (see Figure 47).

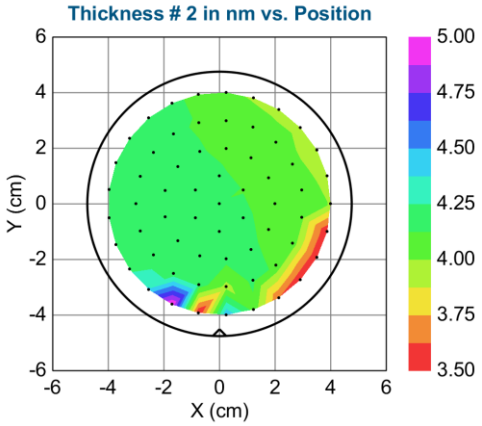

Figure 47a: *7ML MoS_2 thickness uniformity across a 4-inch Si wafer*

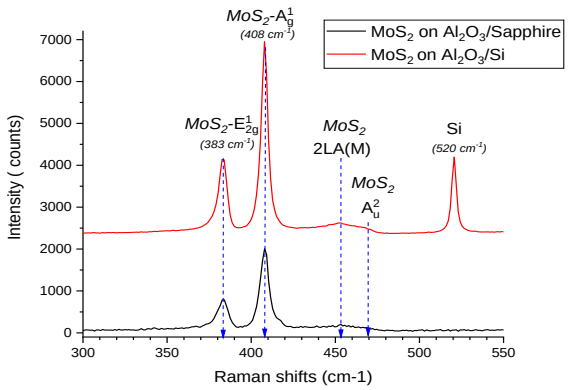

Figure 47b: *Characteristic Raman spectra for 7ML Mc*

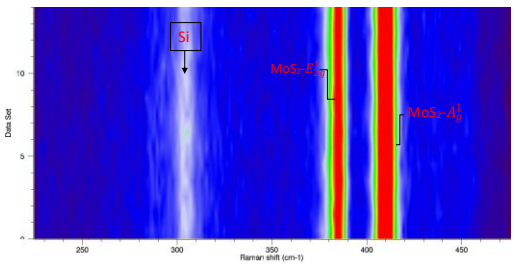

Figure 47c*: 2D Raman mapping 7ML MoS_2 on Si*

TNI-UCC plan to investigate the control of phase transition between 1T' and 2H phases of few-layers MoS_2 in collaboration with NANOTEC and TEOX in Year 2 of PHEMTRONICS project.

[33] M.Dragoman, M.Modreanu et al, Multifunctionalities of 2D MoS_2 self-switching diode as memristor and photodetector, Physica E, 126, 114451, 2021, https://doi.org/10.1016/j.physe.2020.114451

8.2 Molybdenum Oxide, MoOx, as phase change material candidate.

Within PHEMTRONICS we are also investigating layered molybdenum oxides, MoO_x, as a phase change material candidate. In sub-stoichiometric MoO_3, electrical and optical responses across the solar spectrum are tunable and manifest a sharp phase transition in thin films at a specific oxygen content, as different phases are possible as indicated by the diagram in Figure 48 built using the various available data in literature.[34]

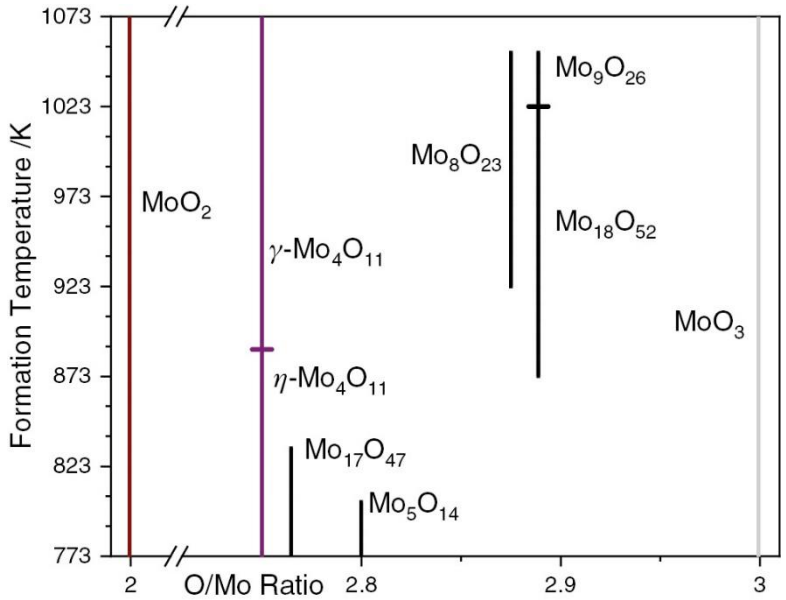

Figure 48: *Phases of the binary system molybdenum-oxygen and their formation temperatures.*

In particular, of interest here are two types of molybdenum oxide, molybdenum trioxide (MoO_3) and molybdenum dioxide (MoO_2) that have an insulator/semi-insulating behavior. Previous report[35] outlines that are at least 5 order of magnitude difference in electrical conductivities between orthorhombic MoO_3 and monoclinic MoO_2, whose structures are shown in Figure 49. The semiconducting-to-metallic transition associated to the MoO_3-to-MoO_2 transition accompanies with a large change of the optical properties as shown by the refractive index, n, and extinction coefficient, k, we have measured by ellipsometry on samples of different oxygen-content and shown in Figure 50.

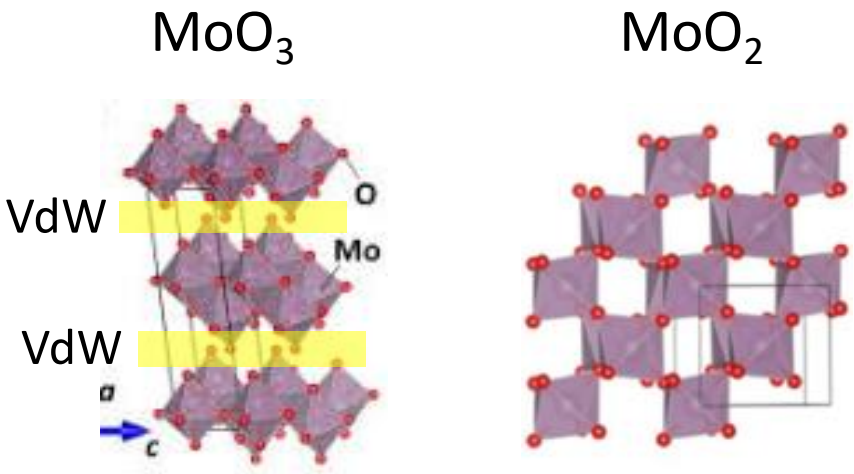

Figure 49*: Structures of layered semiconducting MoO_3 and of metallic MoO_2*

[34] L. Kihlborg, *Acta Chem. Scand.***1959**, *13*, 954. L. Kihlborg, *Adv. Chem.***1963**, *39*, 37.
[35] D. Austin et al, Laser writing of electronic circuitry in thin film molybdenum disulphide, https://doi.org/10.1016/j.mattod.2020.09.036

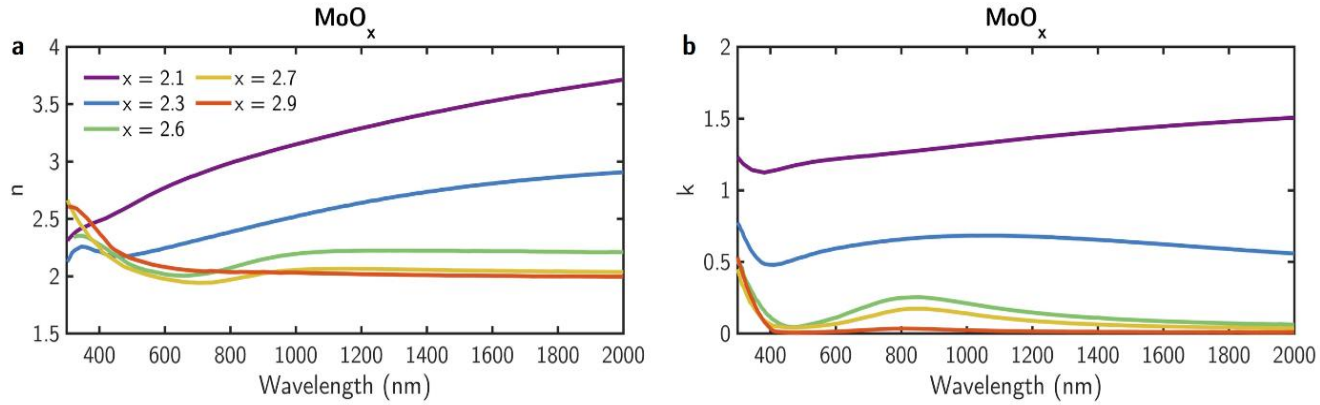

***Figure 50**: (a) Refractive index and (b) extinction coefficient of MoOx layers with different oxygen content, showing the semiconducting (MoO_3) to metallic (MoO_2) transition*

Within PHEMTRONICS have developed a room temperature e-beam evaporation growth process for MoO_3 that offers the flexibility to use a variety of up to 4-inch substrates such as silicon, fused silica, or sapphire. To facilitates the phase transition to MoO_2 the MoO_3 thin films are grown slightly oxygen-deficient as MoO_{3-x}.

In Figure 51 are shown characteristic AFM images for 150nm-thick MoO_{3-x} grown on 4-inch Si substrate. We can have observed from Figure 51 that 150nm-thick MoO_{3-x} assume a nearly atomically smooth surface that is high beneficial for device application.

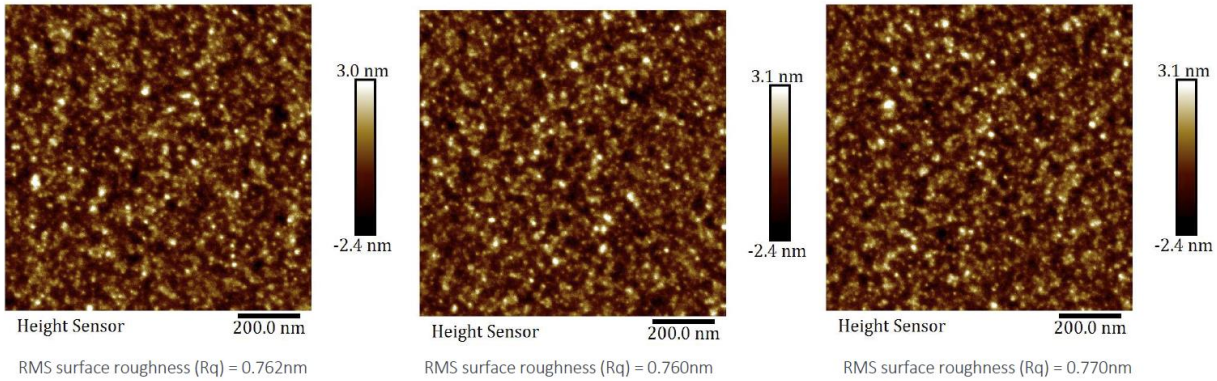

***Figure 51:** 2D AFM images for 150nm-thick MoO_{3-x} grown on 4-inch Si substrate (three sites)*

The Mid to Far IR spectra for 150nm-thick MoO_{3-x} grown on Si by RT E-beam are shown in Figure 49 along with an ATR spectrum for bulk MoO_3. The results presented in Figure 52 indicate that 150nm-thick MoO_{3-x} are amorphous and this was further confirmed from XRD analysis and Raman measurements.

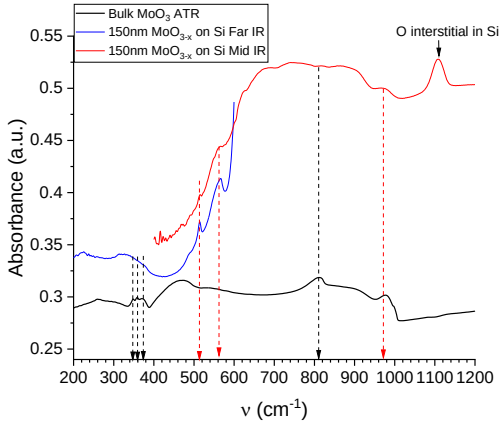

***Figure 52:** Mid to Far IR spectra for a) 150nm-thick MoO_{3-x} grown on Si, and b) bulk MoO_3. The three MoO_3 IR phonon modes located between 300 and 400cm^{-1} are indicative for orthorhombic MoO_3 phase*

The two different approaches of thermal annealing and laser irradiation are being explored in PHEMTRONICS for the MoO_3/MoO_2 phase transformation. Figure 53 shows the picture of large area samples of amorphous MoO_3 as deposited and after annealing in air at 500°C with the corresponding AFM topographies clearly showing crystallization. The measured UV-VIS-NIR optical transmittance in normal incidence for 150nm-thick MoO_{3-x} *as-deposited* and after annealing indicated that the MoO_{3-x} had high transparency across the whole spectral range that significantly decreases after annealing.

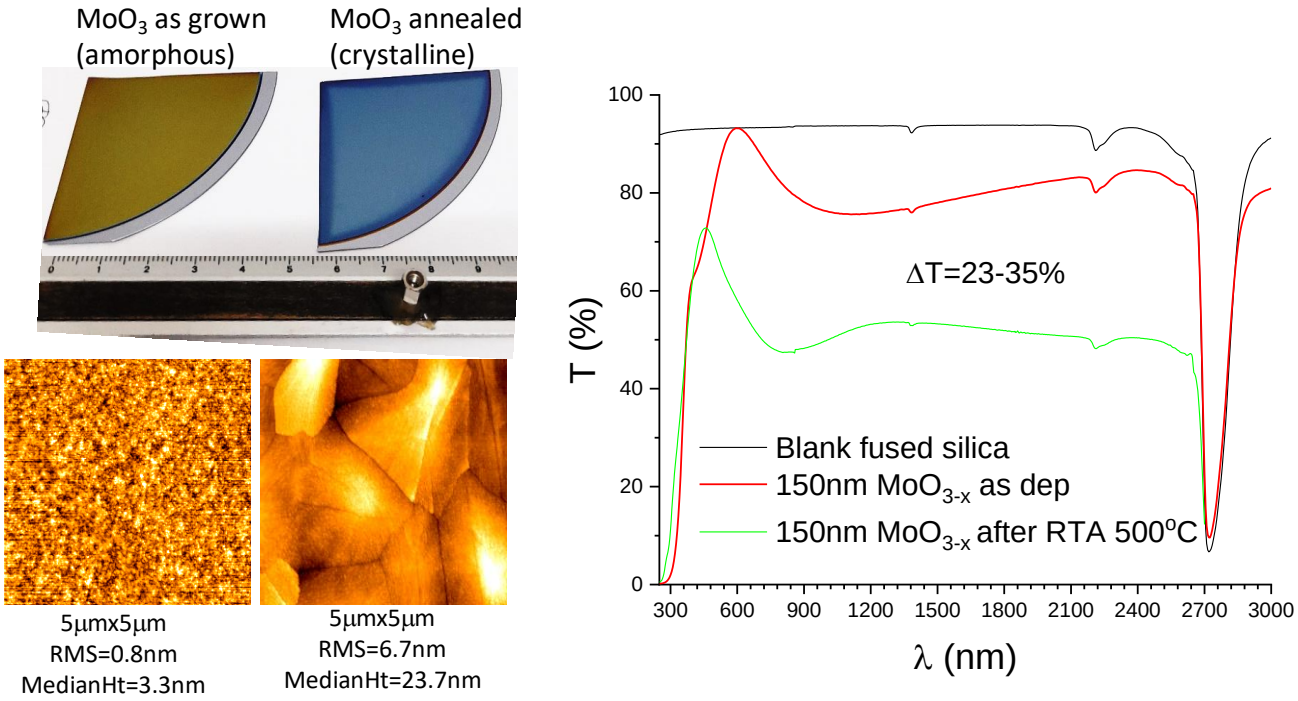

Figure 53: *Pictures of MoOx samples after deposition (left)-amorphous and after annealing in air (right)-crystalline, with corresponding AFM morphologies, showing the formation of crystalline grains. UV-VIS-NIR optical transmittance in normal incidence for 150nm-thick MoO_{3-x} as-deposited and after an RTA at 500°C in air*

Within PHEMTRONICS, we have developed annealing processes, tuning the annealing atmosphere and the temperature, able to operate reversibly the following phase transformations:

a-MoO_3 ↔ c-MoO_3
a-MoO_2 ↔ c-MoO_2
a-MoO_3 ↔ a-MoO_2
c-MoO_3 ↔ c-MoO_2

Those phase transformations have been characterized by x-ray diffraction, AFM, Raman, reflectance and transmittance and Ellipsometry. Some of those data are summarized in Figure 54. In the ellipsometric spectra, the semiconducting-MoO_3 to metallic MoO_2 tranformation is clearly seen in the appearance in the spectra of a Drude metallic component.

Furthermore, the deposited MoOx film shows a large electrical resistance drop of much more than 104-fold at over 350 °C. Such a large drop in electrical resistance was found to be caused by a phase transition from an amorphous state to a crystalline state. It was confirmed that a W/Mo-oxide/W device shows a typical resistive switching effect of a phase change random access memory material and exhibits reversible resistive switching by the application of unidirectional set and reset voltage. The resistance contrast of the device had a large value of about 105–106. Furthermore, the Mo-oxide film showed much better thermal stability in the amorphous state than conventional phase change materials. These results indicate that the Mo-oxide film is a promising oxide-base phase change material for phase change random access memory.

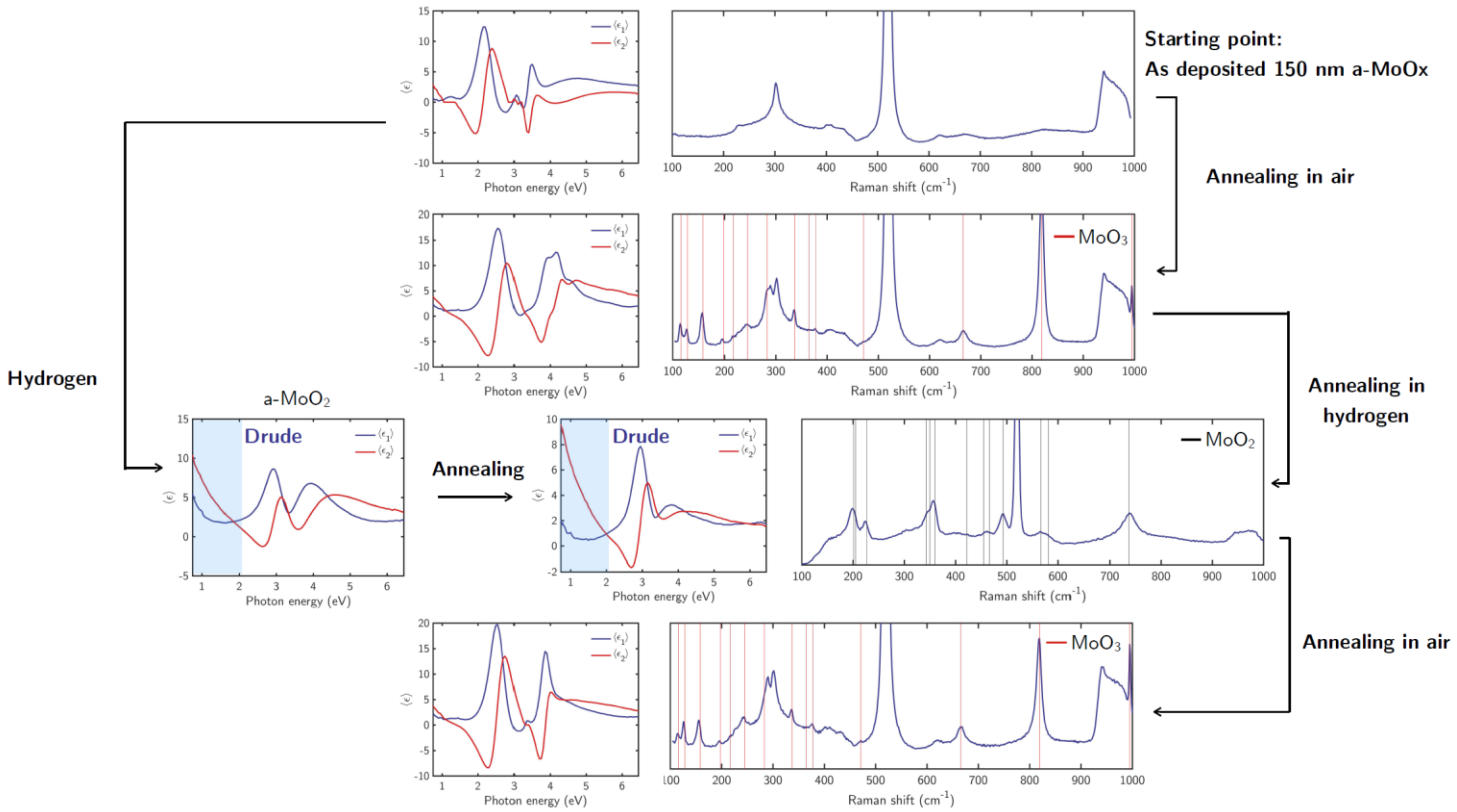

Figure 54: *Raman and ellipsometric spectra of an amorphous deposited 150 nm thick MoO_3 sample that by annealing in various atmospheres is converted to crystalline MO_3 and/or crystalline MoO_2.*

On the basis of those phase-change results, MoOx has been selected as another promising phase-change materials for further optimization.
This is also under consideration of PHEMTRONICS PATENT FILING with applications for dynamic reflective displays

9. Conclusions

Herein, we have reported the research progress in the phase transition, structural and optical properties of several new classes of layered materials under consideration in PHEMTRONICS as optical phase change materials at the telecom wavelength and at optical frequencies to achieve modulation based exclusively on the real part of the material refractive index, free from the loss penalty.

We have been investigated the following classes of 2D materials:

- Group-III Chalcogenides (GaS, GaSe, GaTe)
- Group-V Chalcogenides (Sb, Sb_2S_3, Sb_2Se_3)
- Group-IV Chalcogenides (GeS, GeSe)
- Transition Metal Dichalcogenides (TMDs) (MoS_2, MoOx)

Those materials have been synthesized by various methodologies, both in the amorphous and in the crystalline phase.

We have focused on enabling a phase transition by thermal annealing and laser irradiation, and in characterizing the variation in the structure and corresponding electronic and optical properties.

Various emerging strategies of annealing and laser irradiation have been employed to trigger the structure transition from semiconductor to metallic and stabilize the metallic phase, from amorphous to crystalline phase and viceversa.
Numerous efforts on the phase transition and controlling its reversibility are necessary to understand the correlation between structures, optical properties and real applications.

Being layered materials, their optical properties, namely the dielectric function, was in most cases unknow. Therefore, we have been determining the dielectric function of those materials and its dependence on the number of layers. This will result in an optical database that will be delivered by PHEMTRONICS.

Among the investigated materials, on the basis of the extensive characterization carried out and on the basis of the phase transition presented, the PHEMTRONICS CONSORTIUM has selected the following optical PCMs to be optimized in the next phase:

- GaS and its ternary alloys GaSSe
- Sb_2S_3
- GaSbS
- GeS
- MoOx